U.S. Department of Energy/ Small Business Innovation Research

DOE SBIR Grant No: **DE-SC-0017746**

Development and Advanced Analysis of Dynamic and Static Casing Strain Monitoring to Characterize the Orientation and Dimensions of Hydraulic Fractures

Final Report

Dr. Michael S. Bruno (PI)

msbruno@geomechanicstech.com

GeoMechanics Technologies
103 E. Lemon Ave.,
Monrovia, CA 91016
Phone: 626 305-8460
Fax: 626 305-8462

April 11th, 2017

DUNS Number: 848908356

Project Period: June 12th to April 11th, 2017

Table of Contents

List of Figures

List of Tables

1. Summary

Horizontal wells combined with multi-stage hydraulic fracturing have been applied to significantly increase production from low permeability formations, contributing to expanded total US production of oil and gas. Not all applications are successful, however. Field observations indicate that poorly designed or placed fracture stages in horizontal wells can result in significant well casing deformation and damage. In some instances, early fracture stages have deformed the casing enough so that it is not possible to drill out plugs in order to complete subsequent fracture stages. Improved fracture characterization techniques are required to identify potential problems early in the development of the field.

Over the past decade, several new technologies have been presented as alternatives to characterize the fracture geometry for unconventional reservoirs. Monitoring dynamic casing strain and deformation during hydraulic fracturing represents one of these new techniques. The objective of this research is to evaluate dynamic and static strains imposed on a well casing by single and multiple stage fractures, and to use that information in combination with numerical inversion techniques to estimate fracture characteristics such as length, orientation and post treatment opening.

GeoMechanics Technologies, working in cooperation with the Department of Energy, Small Business Innovation Research through DOE SBIR Grant No: DE-SC-0017746, is conducting a research project to complete an advanced analysis of dynamic and static casing strain monitoring to characterize the orientation and dimensions of hydraulic fractures.

This report describes our literature review and technical approach. The following conclusions summarize our review and simulation results to date:

- A literature review was performed related to the fundamental theoretical and analytical developments of stress and strain imposed by hydraulic fracturing along casing completions and deformation monitoring techniques.

- Analytical solutions have been developed to understand the mechanisms responsible for casing deformation induced by hydraulic fracturing operations.

- After reviewing a range of casing deformation techniques, including fiber optic sensors, borehole ultrasonic tools and electromagnetic tools, we can state that challenges in deployment, data acquisition and interpretation must still be overcome to ensure successful application of strain measurement and inversion techniques to characterize hydraulic fractures in the field.

- Numerical models were developed to analyze induced strain along casing, cement and formation interfaces. The location of the monitoring sensor around the

completion, mechanical properties of the cement and its condition in the annular space can impact the strain measurement.

- Field data from fiber optic sensors were evaluated to compare against numerical models. A reasonable match for the fracture height characterization was obtained. Discrepancies in the strain magnitude between the field data and the numerical model was observed and can be caused by temperature effects, the cement condition in the well and the perturbation at the surface during injection.

- To avoid damage in the fiber optic cable during the perforation (e.g. when setting up multi stage HF scenarios), oriented perforation technologies are suggested. This issue was evidenced in the analyzed field data, where it was not possible to obtain strain measurement below the top of the perforation. This presented a limitation to characterize the entire fracture geometry.

- The comparison results from numerical modeling and field data for fracture characterization shows that the proposed methodology should be validated with alternative field demonstration techniques using measurements in an offset observation well to monitor and measure the induced strain. We propose to expand on this research in Phase II with a further study of multi-fracture characterization and field demonstration for horizontal wells.

2. Background and Introduction

Horizontal wells combined with multi-stage fracturing technology have contributed to a significant increase in oil and gas production from reservoirs throughout the US. Results are often uneven across a field or between wells, however, due to limited control and understanding of fracture orientation, length, and width.

There is limited understanding and few effective diagnostic tools available to characterize the actual fracture placed around the well, particularly in unconventional and naturally fractured formations. Current methodologies to determine fracture dimensions can be divided into 3 groups: direct far field fracture diagnostic techniques including surface and downhole tiltmeter fracture mapping and micro-seismic fracture mapping (Cipolla and Wright, 2000); direct near-wellbore techniques which consist of techniques such as tracer log, temperature logging, production logging, borehole image logging, downhole video and caliper logging (Zemanek, 1969); and indirect fracture techniques consist of hydraulic fracture numerical modeling of net pressure, pressure transient test analyses and production data analyses (Ekie et al. 1977; Tiab et al. 1989). The indirect fracture diagnostic techniques are the most widely used for determining the shape and dimensions of the created fracture, however, the solution from most of the current indirect techniques may not be unique and may require as much fixed data and assumptions as possible.

Monitoring dynamic casing deformation during hydraulic fracturing represents a new technique to characterize the fracture geometry. Research has been found that poorly designed or placed fracture stages in horizontal wells can result in well casing deformation and damage. In many instances, early fracture stages have deformed the casing enough so that it is not possible to drill out plugs in order to complete subsequent fracture stages. GeoMechanics Tech has analyzed well deformation and damage related to fractures that extend at oblique angles to the horizontal wellbore. The results from preliminary numerical modeling combined with field observations suggest that deformation is highly dependent on fracture angle, opening displacement, and length. No work regarding using the information of casing deformation during hydraulic fracturing to characterize the fracture has been published.

The objective of this research is to develop and demonstrate with field data a more accurate and cost-effective technique to estimate fracture height, length, and orientation than currently available technology. We propose to develop and investigate advanced techniques to analyze dynamic micro-deformation and static large strain deformation in wellbore casing during and after hydraulic fracture operations to characterize the orientation, width, and extent of created fractures. The initial DOE research project efforts include:

1. A review and documentation of the theory and analysis of stress and strain imposed on casing by hydraulic fracture operations;
2. Review and document techniques to measure dynamic and static strain in casing systems that are induced by hydraulic fracture operations;
3. Develop and demonstrate the use of numerical modeling and inversion techniques to use measured casing strain to characterize the orientation, length, and opening displacement of single and multiple fractures;
4. Compare and demonstrate the effectiveness and application of the analytical and numerical techniques developed with actual field data;
5. Documentation of results in this technical report.

Successful development and demonstration of this new technique can provide industry with a more cost-effect and improved technique to characterize single and multiple fractures in a wide range of geologic conditions. This information can lead to more effective production and more reliable evaluation of environmental risks, including enhanced protection of potential USDWs.

3. Theoretical and Analytical Developments and Documentation (Project Task 2)

Before describing the fundamental theoretical and analytical developments that represent the stress and strain imposed by hydraulic fracturing along casing completions, it is important to understand the mechanisms responsible for casing deformation.

Zhaowei et al. (2016) presented a study of the mechanisms of casing deformation in the Changninge Weiyuan national shale gas demonstration area and countermeasures. Various mechanisms of casing deformation were identified. For instance, fracturing fluid moves into natural fractures through flowing channels and consequently boosts pore pressure inside the fractures. When pore pressure reaches a critical value, fracture planes may be motivated to slide, which results in casing deformation. The flowing channel may be hydraulic fractures (Figure 1-a), axial fractures generated by hydraulic fracturing along the wellbore (Figure 1-b), or micro-annuli at the second interface of the cement sheath (Figure 1-b).

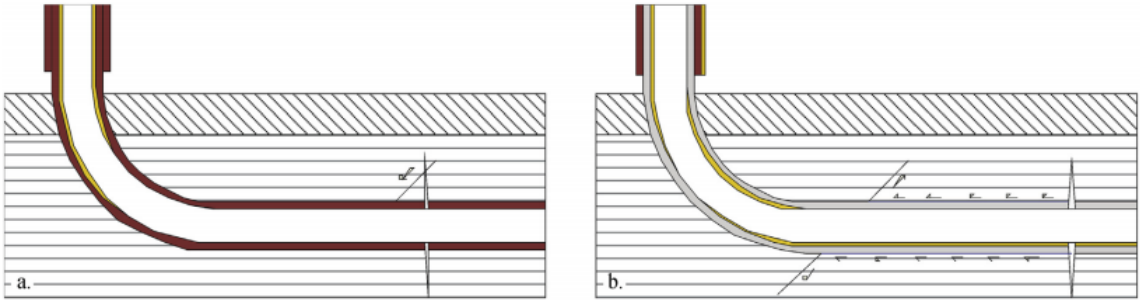

Figure 1: Diagram showing casing deformation during hydraulic fracturing (After Zhaowei et al, 2016).

Some variables that can impact casing deformation include mechanical conditions of fracture-plane sliding, flowing channels, axial fractures along the borehole created during hydraulic fracturing and micro-annulus between cement sheath and wall rocks.

When the inner casing pressure is loaded during hydraulic fracturing, the casing will expand outward and deform the cement sheath and wall rocks. If the pressure is large enough, the cement sheath will experience plastic deformation that cannot be recovered. If the pulling stress is larger than the interfacial cementing strength, intermediate micro-annulus deformation will occur. The prerequisite for micro-annulus deformation is the plastic deformation of cement sheath, which may be induced by a large bottom hole pressure during hydraulic fracturing. Thus, casing deformation located far away from perforation points may be related to micro-annuli and axial fractures.

Lian et al. (2015), presented a study on casing deformation failure during multi-stage hydraulic fracturing for the stimulated reservoir volume for horizontal shale wells. The research results indicate: 1) the stress deficit of zero stress areas and tension stress areas occurred within the range of stimulated reservoir volume during the process of volume fracturing. And, the state of this stress deficit, which would make clustering perforation casings of horizontal wells "hanging" in the formation to some extent, resulted in certain degree of deflection deformation radically and S-shape deformation axially; 2) the problem of casing deformation failure remains fundamentally unsolvable through simply improving casing grade and wall thickness to increase flexural strength and; 3) the key to solving casing deformation failure is the reasonable spacing design of multi-stage fracturing. Figure 2 shows an example of casing deformation after the 6th stage fracturing varied with well depth.

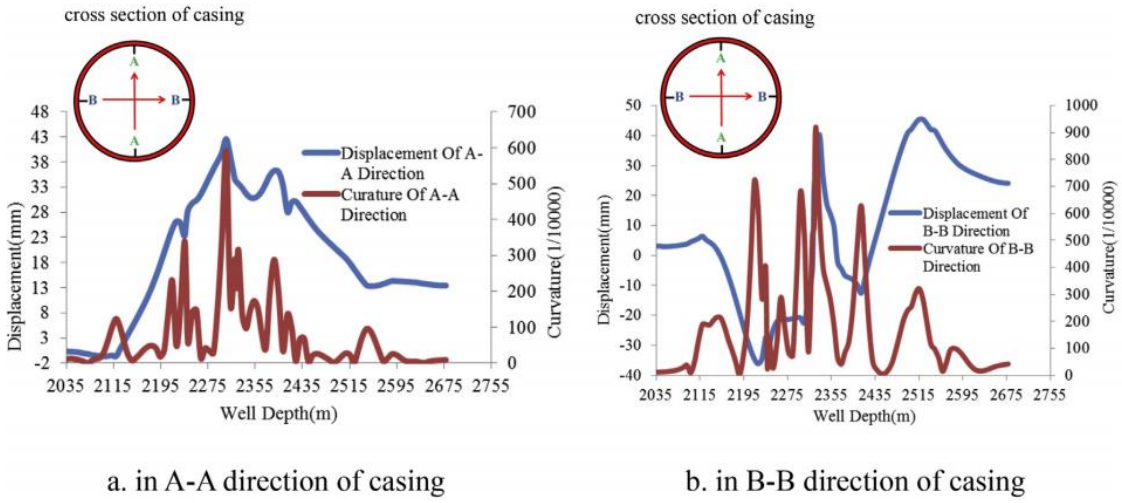

a. in A-A direction of casing b. in B-B direction of casing

Figure 2: Example of casing deformation after 6th staged fracturing varied with well depth (After Lian et al, 2015).

Lin et al. (2017) presented a case study of a shale gas well with casing failure during volume fracturing. They stated that a large number of casing failures occur during the volume fracturing operation of shale gas, making normal completion stimulations impossible. Their results indicated that the obtained mechanism of casing failure is elliptical deformation of casing section. Oversize ovality leads to sticking of subsequent run tools. A comparison with the field MIT logging data verified the effectiveness of the method used and the accuracy of calculations. In addition, increasing wall thickness is more effective to improve the resistance to ovality than increasing steel grade. Also, the reasonable spacing design of volume fracturing can help solve casing deformation failure. Figure 3 presents a comparison example of casing deformation simulated during volume fracturing and Multi-arm Caliper Imaging Tool (MIT) logging data varied with well depth.

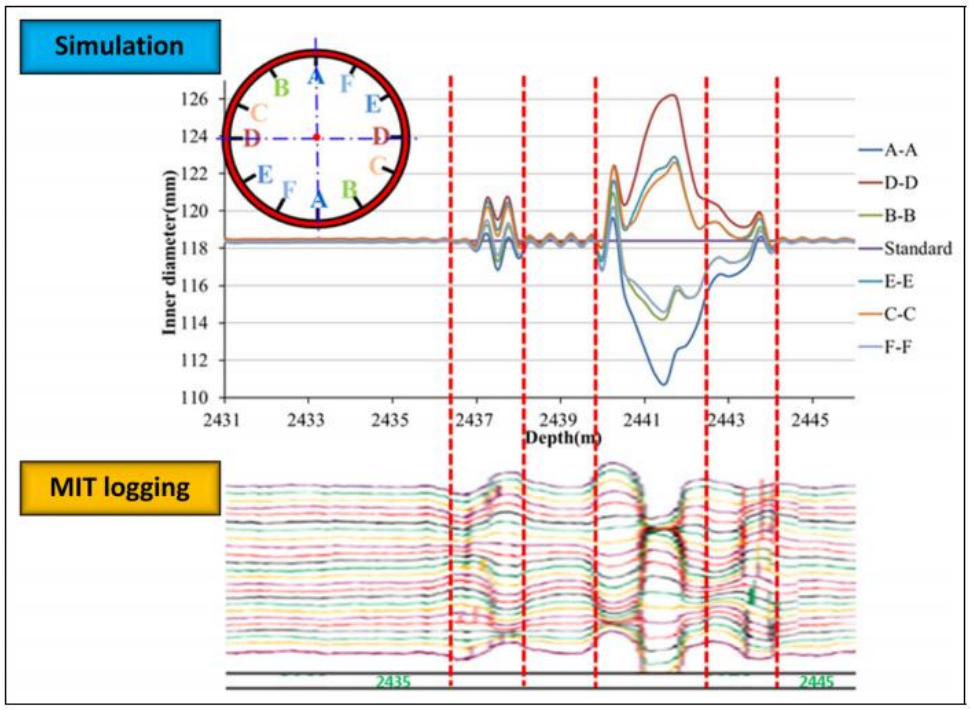

Figure 3: Comparison example of casing deformation simulated and Multi-arm Caliper Imaging Tool (MIT) logging data varied with well depth (After Lin et al, 2017).

After discussing the fundamental mechanisms responsible for casing deformation, we now describe the theory and analytical expressions of stress and strain imposed by hydraulic fracture operations along casing completions, underground discontinuities and surface uplift. For this case, our main objective is to focus on the analysis of induced displacements and stresses caused by unconventional hydrofracture boreholes, considering the surrounding deformation around fractures and casing completions to characterize its orientation, potential width, length and height applying inversion techniques.

To understand induced deformation associated with hydraulic fracturing, analytical models have been reviewed. Davis (1983) provided expressions for crustal deformations induced by hydro fracturing considering a dipping rectangular dislocation beneath the surface of an elastic half space. The movements of dislocations are represented by Burgers vector. This vector represents the magnitude and direction of the lattice distortion resulting from a dislocation in a crystal lattice as presented in Figure 4 (Callister W, 2005). In edge dislocations, the Burgers vector and dislocation line are perpendicular to one another and in screw dislocations, they are parallel (Kittel C, 1996).

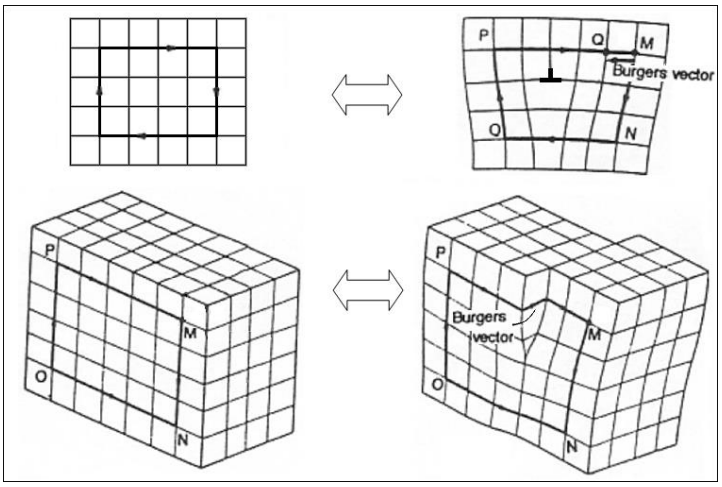

Figure 4: Burgers vector. Top right is an edge dislocation and bottom right is a screw dislocation (After Callister W, 2005).

Davis (1983) considered Burgers vector normal to the dislocation rectangular surface in problems where the crust is intruded, such as sill and dike injections in volcanic zones, including the mid-ocean ridges and continental rifts, or hydrofractures as induced to stimulate oil or geothermal reservoirs. He obtained analytical expressions for vertical displacements from integration of Volterra's equation by using Mindlin's point force solutions for the elastic half space. This equation is expressed as follows (Steketee, 1958):

$$u_i = \iint_{\Sigma}^{\cdot} b_j \left[\delta_{jk}\lambda \frac{\partial U_{il}}{\partial \xi_l} + \mu\left(\frac{\partial U_{ij}}{\partial \xi_k} + \frac{\partial U_{ik}}{\partial \xi_j}\right)\right] v_k ds \qquad \textit{Eq. 1}$$

where the integral is taken over the dislocation surface, u_i is the displacement in the X_i direction at a point (X_1, X_2, X_3). U_{ij} is the *i*th component of displacement at (X_1, X_2, X_3) owing to a point force of unit magnitude acting in the *j* direction at a point (ξ_1, ξ_2, ξ_3) on Σ within an elastic half space. The Lamê coefficients are λ and μ, and v_k is the normal to Σ at (ξ_1, ξ_2, ξ_3). For a sloping rectangular surface of dip δ, the dislocation geometry and coordinate system is presented in Figure 5.

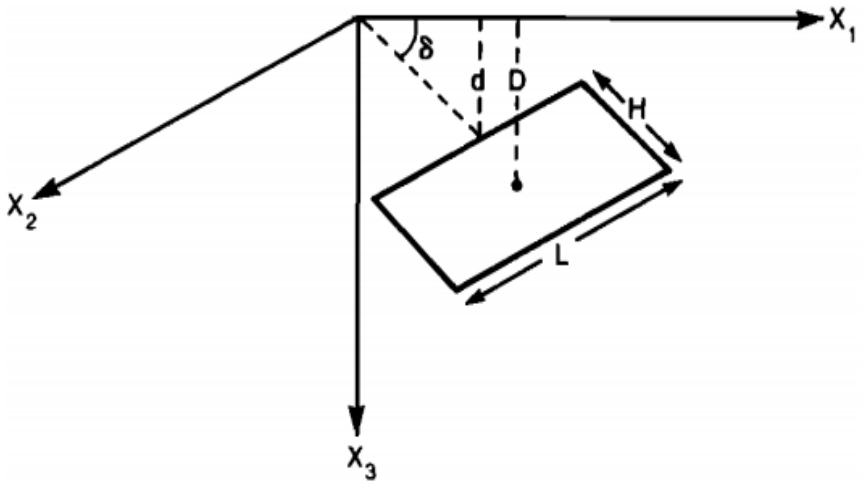

Figure 5: Dislocation geometry and coordinate system (After Davis, 1983).

The displacement field produced by dislocation of magnitude *b* normal to its surface is:

$$u_i = \iint_{\Sigma}^{\cdot} b \left\{ \lambda \frac{\partial U_{il}}{\partial \xi_l} + 2\mu \frac{\partial U_{il}}{\partial \xi_1} sin^2\delta + 2\mu \frac{\partial U_{i3}}{\partial \xi_3} cos^2\delta - 2\mu \, sin\delta \, cos\delta \left(\frac{\partial U_{i1}}{\partial \xi_3} + \frac{\partial U_{i3}}{\partial \xi_1} \right) \right\} ds \qquad Eq.\ 2$$

If coordinate ξ is measured positive down the fault dip, $ds = d\xi_2 \; d\xi$, so that the rectangular surface given by $-l \le \xi_2 \le l$, $H/2 \le \xi \le H/2$, has length, $L = 2l$ and height H.

In addition, Davis (1983) presented two examples, one of a near horizontal and one of a near vertical fracture. Using nonlinear inversion of surface tilt fields associated with hydrofracture of deep boreholes, fracture geometry, position, and orientation along with their uncertainties were estimated. He showed that this model can approximate well a tensile crack, just as shear dislocations are successfully used to approximate the deformation fields by shear cracks.

Okada Y. (1985) presented a complete suite of closed analytical expressions for the surface displacements, strains, and tilts due to inclined shear and tensile faults in a half-space for both point and finite rectangular sources. He has completed the surface displacement problem, giving all components of surface stresses, strains, and displacements.

Yang X. and Davis P. (1986) presented closed, analytic expressions given for the displacement fields, their derivatives, and stresses from a rectangular crack in an elastic half-space having Burger's vector normal to its surface. The mathematical expression of the displacement field produced by a dislocation b_j across a surface Σ in a uniform elastic half-space was given by Volterra's formula previously describe in **Error! Reference**

ource not found.. A similar dislocation geometry and reference coordinate system described by Davis (1983) was presented in this paper as seen in Figure 6.

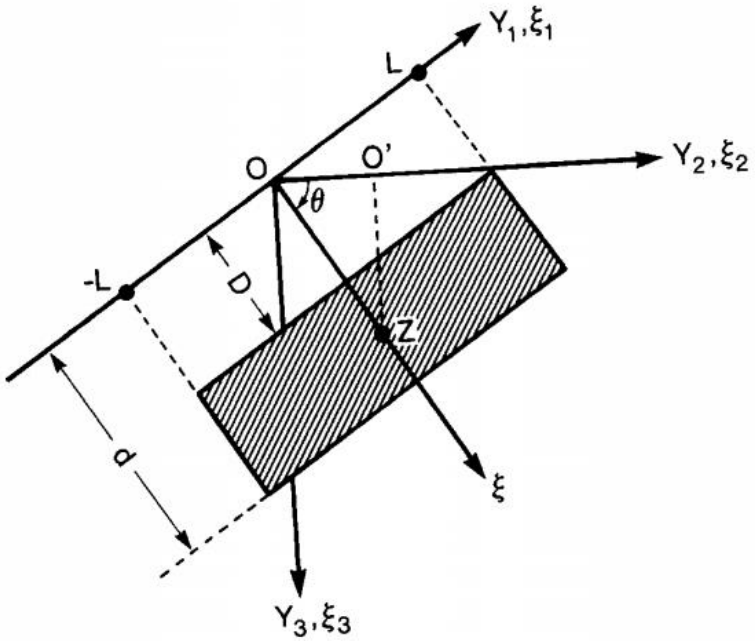

Figure 6: Crack geometry and coordinate system (After Yang and Davis, 1986).

where Σ is the surface, $-L \le \xi_1 \le L$, $d \le \xi \le D$ over which b is constant, and θ is the dip angle.

For convenience, the authors first introduce the following variables before presenting the displacement fields equations (Yang and Davis, 1986):

$X_1 = y_1 - \xi_1$,

$X_2 = y_2 - \xi_2$,

$X_3 = y_3 - \xi_3$,

$\overline{X}_3 = y_3 + \xi_3$,

$t_2 = y_2 \sin\theta - y_3 \cos\theta$,

$t_3 = y_2 \cos\theta + y_3 \sin\theta$,

$q_2 = y_2 \sin\theta + y_3 \cos\theta$,

$q_3 = -y_2 \cos\theta + y_3 \sin\theta$,

$R_1 = \sqrt{{X_1}^2 + {X_2}^2 + {X_3}^2}$,

$R_2 = \sqrt{{X_1}^2 + {X_2}^2 + {\overline{X}_3}^2}$.

Then, using U_{ij} given by Mindlin (1936) and the integration of Eq. *2* gives the displacement fields expressed as (Yang and Davis, 1986):

$$U_1 = \frac{b}{8\pi\,(1-\upsilon)}\left\{4\,(1-\upsilon)(1-2\upsilon)\cdot\ tan^2\theta\ \left(\sin\theta\cdot ln\left(R_2+\overline{X}_3\right)-ln(R_2+\xi+q_3)-\frac{cos\theta\cdot X_2}{(R_2+\overline{X}_3)}\right)-t_2a_1+(q_2-4(1-\upsilon)sin\theta\cdot y_2)\overline{a}_1+(1-2\upsilon)\cdot ln\left(\frac{R_2+\xi+q_3}{R_1+\xi-t_3}\right)-2(1-2\upsilon)\cdot\frac{sin\theta\cdot y_3}{R_2}+2y_3\cdot\left(\frac{y_2q_2}{{R_2}^3}+\frac{y_3}{R_2(R_2+\xi+q_3)}-q_2B\right)\right\}\| \quad \textit{Eq. 3}$$

$$U_2 = \frac{b}{8\pi\,(1-\upsilon)}\left\{4\,(1-\upsilon)(1-2\upsilon)\cdot tan^2\theta\ \left[2sin\theta\cdot tan^{-1}\left(\frac{cos\theta\cdot q_2+(1+sin\theta)(R_2+\xi+q_3)}{cos\theta\cdot X_1}\right)+\frac{cos\theta\cdot X_1}{(R_2+\overline{X}_3)}\right]+4(1-\upsilon)sin\theta\cdot\left[tan^{-1}\left(\frac{X_1+R_1+\xi-t_3}{t_2}\right)+tan^{-1}\left(\frac{X_1+R_2+\xi+q_3}{q_2}\right)\right]-t_2a_3+(q_2-4(1-\upsilon)sin\theta\cdot y_2)\overline{a}_3+(1-2\upsilon)cos\theta\cdot ln\left(\frac{R_1+X_1}{R_2+X_1}\right)-2sin\theta\cdot y_3\frac{(2(1-\upsilon)X_2+\xi_2)}{R_2(R_2+X_1)}-2sin\theta\cdot y_3(X_1A-X_1B)\right\}\| \quad \textit{Eq. 4}$$

$$U_3 = \frac{b}{8\pi\,(1-\upsilon)}\left\{-8\,(1-\upsilon)(1-2\upsilon)\cdot sin\theta\cdot tan\theta\cdot tan^{-1}\left(\frac{cos\theta\cdot q_2+(1+sin\theta)(R_2+\xi+q_3)}{cos\theta\cdot X_1}\right)-4(1-\upsilon)cos\theta\cdot\left[tan^{-1}\left(\frac{X_1+R_1+\xi-t_3}{t_2}\right)+tan^{-1}\left(\frac{X_1+R_2+\xi+q_3}{q_2}\right)\right]-t_2a_2+(q_2+4(1-\upsilon)sin\theta\cdot y_2)\overline{a}_2+(1-2\upsilon)sin\theta\cdot ln\left(\frac{R_1+X_1}{R_2+X_1}\right)-2sin\theta\cdot y_3\frac{(2(1-\upsilon)\overline{X}_3+\xi_3)}{R_2(R_2+X_1)}-2y_3\left(sin\theta\cdot\overline{X}_3A-cos\theta\cdot X_1B\right)-8(1-\upsilon)sin\theta\cdot y_3\overline{a}_3+2y_3X_1\left(\frac{q_3}{{R_2}^3}-\frac{1}{R_2(R_2+\xi+q_3)}\right)+2sin\theta\left(\frac{X_1}{R_2}+\frac{\xi(\xi+q_3)}{R_2(R_2+X_1)}-\frac{X_1q_3}{R_2(R_2+\xi+q_3)}\right)\right\} \quad \textit{Eq. 5}$$

where

$$a_1 = \frac{t_2}{R_1(R_1+\xi-t_3)},$$

$$\overline{a}_1 = \frac{q_2}{R_2(R_2+\xi+q_3)},$$

$$a_2 = \frac{cos\theta\cdot X_1}{R_1(R_1+\xi-t_3)}-\frac{X_2}{R_1(R_1+X_1)},$$

$$\overline{a}_2 = \frac{-cos\theta\cdot X_1}{R_2(R_2+\xi+q_3)}+\frac{X_2}{R_2(R_2+X_1)},$$

$$a_3 = \frac{-sin\theta\cdot X_2}{R_1(R_1+\xi-t_3)}+\frac{X_3}{R_1(R_1+X_1)},$$

$$\overline{a}_3 = \frac{-sin\theta\cdot X_1}{R_2(R_2+\xi+q_3)}-\frac{\overline{X}_3}{R_2(R_2+X_1)},$$

$$A = \frac{X_1}{{R_2}^3}-\frac{1}{R_2(R_2+X_1)}+\frac{\xi(\xi+q_3)(2R_2+X_1)}{{R_2}^3(R_2+X_1)^2},$$

$$B = \frac{-cos\theta\cdot q_3}{{R_2}^3}+\frac{cos\theta}{R_2(R_2+\xi+q_3)}+\frac{sin\theta\cdot q_2\cdot q_3(2R_2+\xi+q_3)}{{R_2}^3(R_2+\xi+q_3)^2}$$

where υ is Poisson's ratio, and $||$ represent the integral limits for the variables ξ_1 and ξ. Derivatives of U_i with respect to y_j are obtained by using computational subroutine to calculate strain and stress with the following expressions (Yang and Davis, 1986):

$$e_{ij} = \frac{1}{2}\left(\frac{\partial U_i}{\partial y_i} + \frac{\partial U_j}{\partial y_i}\right) \quad \textit{Eq. 6}$$

$$\sigma_{ij} = \lambda e_{kk}\delta_{ij} + 2\mu e_{ij} \quad \textit{Eq. 7}$$

4. Review and Summary of Casing Deformation Monitoring Techniques (Task 3)

Given the range of anticipated deformation induced by various types and numbers of hydraulic fractures, the next step in the process is to review and summarize casing deformation monitoring techniques. This will help this research project and others to determine the requirements and most effective approaches for monitoring.

There are several methods to monitor casing deformation in either real-time during fracture treatment or post treatment. These include mechanical caliper technologies, electromagnetic detection technology, ultrasonic detection, etc. (Sun, B. et al, 2014). Additional deformation measurement techniques include combined multi-finger imaging and magnetic thickness tools, cross multipole array acoustic technology, borehole ultrasonic imaging, and fiber optic sensors (Zhou, Z. et al, 2009). These generally measure only large-scale deformation.

Monitoring very small strain deformations require higher accuracy, resolution, and sensitivity that can be obtained using electronic and fiber-optic type sensors. The primary advantages of fiber optic sensors include high-speed data transmission, smaller cable to carry the same information, no issues related to electrical noise and high bandwidth capacity (Harold, L., 2005). Fiber optic sensors can be embedded in composite materials in a nonobtrusive manner that does not degrade structural integrity. In general, the embedded fiber optic sensors can monitor the health of the structures in the service condition. These can be installed as a continuous distributed sensor, quasi-distributed or at a point sensing. Note that distributed monitoring systems are those in which the whole length of a cable is used as a monitoring system, and data can be acquired anywhere along its length, limited only by spatial resolution. Quasi-distributed monitoring systems consist of a dense array of sensors (typically more than 10) that will monitor only the points where the sensors are located (Pinto, H. et al., 2013).

One of the first fiber optic technologies for casing strain monitoring is the Fiber Bragg Grating (FBG) sensor that was originally developed for compaction monitoring. The small size of the FBG sensor allows embedding them in composite structures, while the

multiplexing capability allows, for example, adopting sensors-averaging techniques. These FBG sensors work as strain and temperature sensors: each of the FBG sensors reflect a specific wavelength of the laser, which is influenced by temperature and strain on fiber, making them work as optical strain gauges. The system has thousands of FBG sensors imprinted on a fiber spaced only a few centimeters apart. The fiber is then rolled in a spiral around the casing and the response of each is acquired by an interrogating hardware. The received signal is then analyzed and it is possible to correlate with the type and level of deformation on casing or tubing.

Alternative to FBG sensor technology, there is a Distributed Temperature and Strain Sensor (DTSS) based on Brillouin scattering technology to perform active vibration control. Compared to FBG sensors, distributed optical fiber sensors based on Brillouin scattering do not require any special structure to be fabricated within the fiber (since they use a standard optical fiber) and are intrinsically capable of performing strain measurements in several hundreds or thousands of measuring points simultaneously along the fiber itself. This system is based on a nonlinear characteristic of the fiber optic line: when a laser is pumped through it, a backscatter is detected, due to interaction between the laser and the material of the fiber (Kenichi, S. et al, 2008). Raman backscattering is strongly dependent on temperature and is the basis of the DTS systems commonly used for production monitoring. Brillouin backscattering is strongly dependent both on temperature and strain and is used on the DTSS system (Pinto, H. et al., 2013).

Another technology available for casing micro-deformation monitoring is piezoelectric transducers that can be installed on the surface of the casing or embedded on it. These provide information on stress, strain and corrosion using guided elastic waves (Lamb Waves). This technology is being used in integrity monitoring of aeronautical structures and pipelines. Also, high-resolution ultrasonic imaging systems can be developed to be permanently installed on the production tubing, providing information of geometry, stress and integrity both on cement and casing. These solutions are in the early stages, but could simplify monitoring of well deformation, reducing costs and complexity of installation (Pinto, H. et al., 2013).

A more detailed description on the existent techniques and tools for casing monitoring is presented below:

4.1 Fiber optic sensors

Fiber optic sensing technology was first introduced in the 1990s with single-point pressure and temperature sensors to be applied in the oil and gas industry for downhole applications. Today, there are different types of fiber optic techniques that can vary from a single-point sensor to an array of quasi-distributed point sensor measurements or to a fully distributed sensor, where the entire fiber becomes the sensor as seen in Figure 7. A range of parameters including: temperature, strain, pressure and acoustic measurements can be performed with this technology (Molenaar and Cox, 2013).

The sensors can be used, either temporarily hung in the well or permanently installed as part of the well construction. In the past, electrical point sensors were the only means to measure. Recently developed fiber optic sensors provide a very promising alternative. Fiber optics provide distributed measurements, are passive, potentially low-cost, have a long service life and a small form-factor. It is important to highlight that the inherent long-term reliability of such sensor, combined in a downhole deployable single optical fiber cable makes fiber-optic technology an effective platform for permanent sensing in oil and gas wells. A range of applications including: distributed inflow measurement, sand detection, outflow lift optimization, smart well completion monitoring and more can be performed.

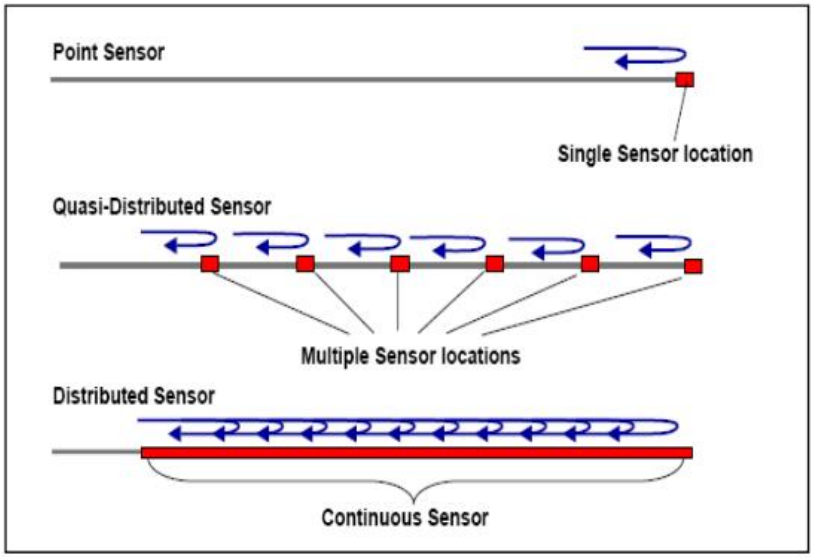

Figure 7: Fiber optic sensing configurations (after Molenaar and Cox, 2013)

As shown in Figure 7, a continuous sensing can be performed by fiber optic distributed sensors. This technology is currently at different stages of development. For example, Distributed Temperature Sensing (DTS) is the most mature technology, with a history of successful downhole applications that dates back 15 years. Distributed Strain Sensing developed by Shell and Baker-Hughes under the product name Real Time Compaction Monitoring (RTCM) and Distributed Acoustic Sensing (DAS) are in the stage of field-testing with promising results. Other distributed sensors include: Distributed Chemical Sensing (DCS) which is a less mature technology and also Distributed Pressure Sensing (DPS) which is being developed (Koelman et al, 2012).

Another important key point in fiber optic analysis is the backscattered light when a pulse of light travel down through an optical fiber. The majority of the light travels through but a small fraction is scattered back at every location of the fiber. As seen in Figure 8, the frequency of this backscattered light is shifted from the original input frequency by an amount linearly proportional to the temperature and strain applied at the scattering

location. By resolving the back-scattered signal in time and frequency, a complete strain profile along the full length of the fiber can be obtained (Soga et al., 2008).
Basically, three different backscatter mechanisms are indicated. For example, *Raman scattering* or *Raman effect*, results in backscattered light at two spectrally shifted wavelengths compared to the incident light. The intensity of the so-called *anti-Stokes* band is temperature-dependent, while the so-called *Stokes* band is practically independent of temperature. *Brillouin Scattering* also results in two side-lobes, however, with wavelengths depending on, e.g., strain or temperature. Brillouin-based fiber optic sensing is mainly used for static strain and temperature measurements. The third scattering mechanism described in Figure 8 is *Rayleigh scattering* which is an elastic scattering of photons, resulting in backscattered energy at the same wavelength as the incident light. Rayleigh scattering is the basis for Distributed Acoustic Sensing (DAS).

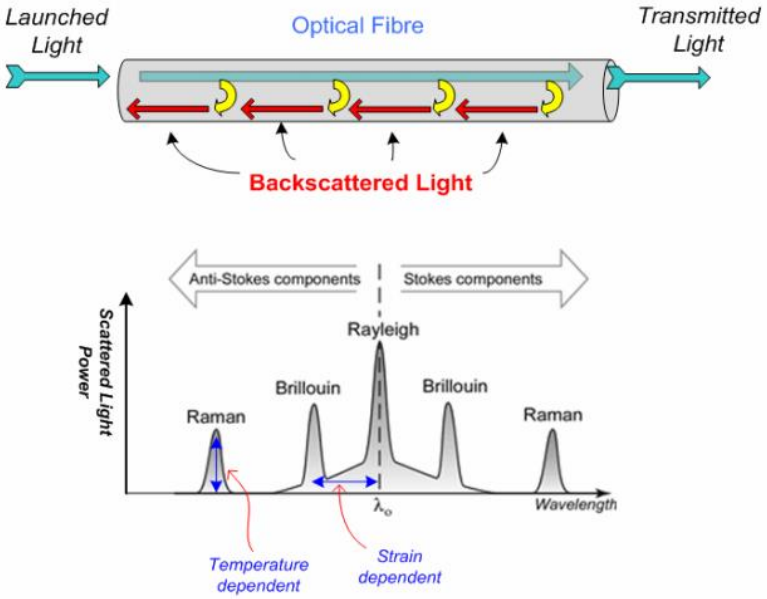

Figure 8: Backscattered light (after Soga et al, 2008).

It is also important to point out that for casing deformation analysis induced by hydraulic fracturing operations, mechanical strain and temperature were considered herein as the main variables to be described. These are grouped based on the different technologies as follows:

4.1.1 Discrete Fiber Optic Sensing

A Fiber Bragg Gratings (FBG) is a discrete sensor that measures a local periodic variation of the refractive index in the core of an optical fiber. FBG sensors are inscribed in a photosensitive fiber by using an intense ultraviolet source, and are typically between 1 and 10 mm long. The periodic refractive index variation, as illustrated in Figure 9-a, leads to a similar effect as seen in atomic crystal layers: Bragg reflection at a wavelength related to the periodicity of the structure. The reflected wavelength will change if the

periodicity or the refractive index changes, as depicted in Figure 9-b. This feature enables the use of FBGs as sensors. For example, see the temperature sensor illustrated in Figure 9-c, which reflects a temperature increase leading to an expansion of the glass and hence to a change in periodicity. Similar, strain on the FBG changes the periodicity as well, therefore a FBG is a strain sensor. This can be exploited as, e.g., a pressure sensor by attaching a FBG to a membrane as presented in Figure 9-d. A chemical sensor can be realized by coating the FBG with a specific polymer which swells when in contact with a specific chemical substance as seen in Figure 9-e (Lumens, 2014).

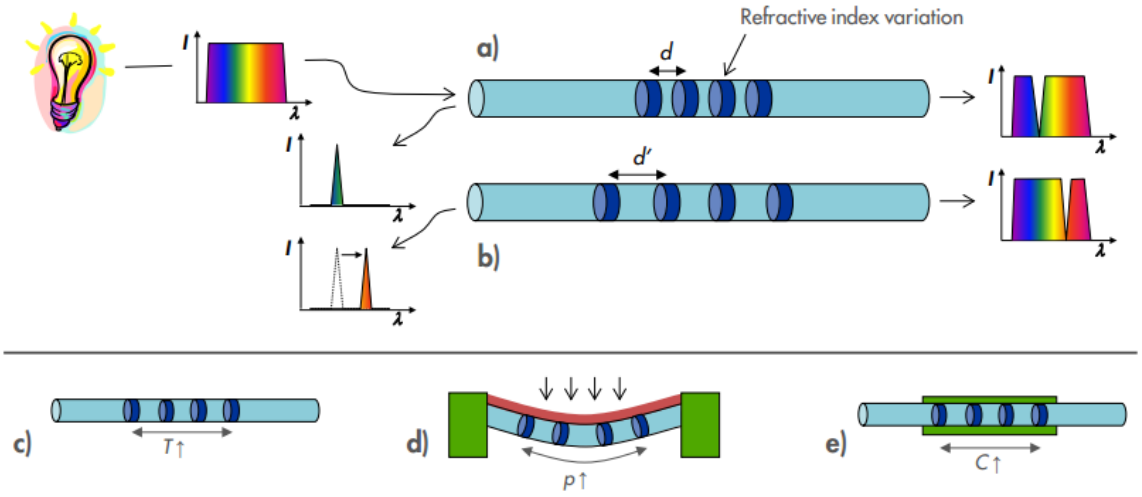

Figure 9: The working principle and some applications of Fiber Bragg Gratings (after Lumens, 2014).

The wavelength of reflected light, λ, is proportional to the grating spacing, D and expressed as follow (Appel et al, 2007):

$$\lambda = 2nD \qquad \textit{Eq. 8}$$

where n is the effective index of refraction of the fiber glass core.

Each grating is basically a strain gauge. When strain is applied to the sensing fiber, the gratings stretch or contract with the fiber, and modify the distance D between the bands of the grating. Based on *Eq. 8*, such modification causes a shift in the wavelength of light reflected off the strained Bragg-grating. This shift is given by (Appel et al, 2007):

$$\Delta\lambda = \lambda(1 - P_e)K\varepsilon_f \qquad \textit{Eq. 9}$$

where $\Delta\lambda$ is the Bragg wavelength shift due to the strain, ε_f, imposed on the fiber. λ is the average wavelength of the grating, and K the bonding coefficient of the fiber to a

substrate or system on which the strain is to be measured. P_e describe the strain effect on the index of refraction of the fiber. For gratings written such that they reflect a wavelength of 1560 nm, the strain-induced wavelength shift of the reflected light corresponds to approximately 1.232 nm per 1000 microstrains (0.1 % strain). An example of strain-induced shift in wavelength of the light reflected off an individual Bragg-grating can be shown in Figure 10. Note that an increase in wavelength of the reflected signal range from 1558.7 to 1561.1 nm implies an applied strain on the fiber of approximately 0.195 % (Appel et al, 2007).

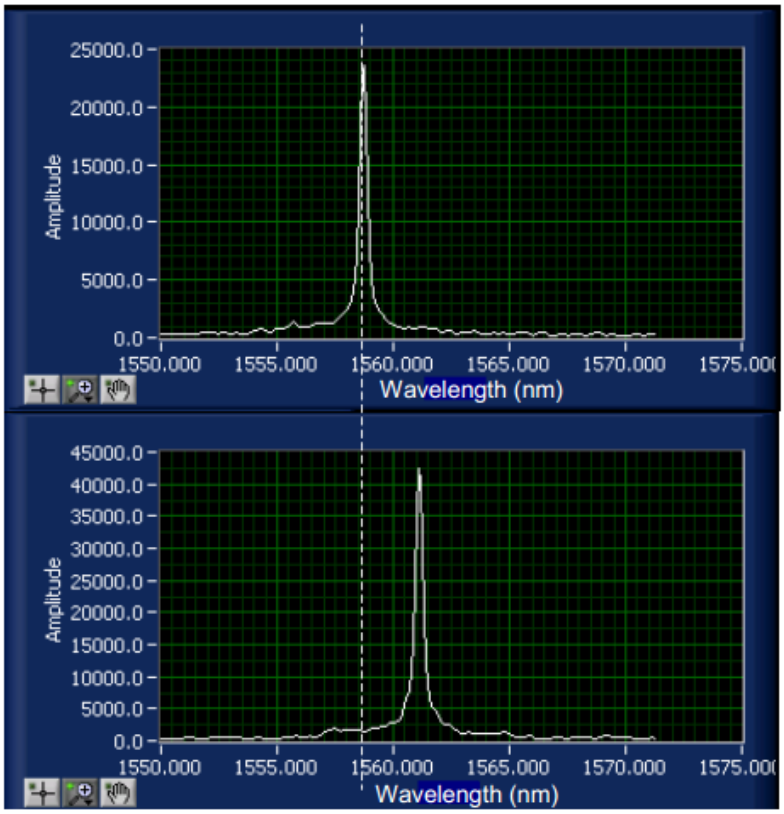

Figure 10: Example of strain-induced shift in wavelength of light reflected off an individual Bragg-grating (after Appel et al, 2007).

After describing the principle of FBG as individual sensing, it is also essential to understand how multiple FBG can be interrogated and their individual response analyzed to characterize the deformation of a long section of well tubular. In principle, this could be achieved by inscribing each FBG with a particular grating spacing, such that each grating would reflect light with a specific wavelength in a process known as *wavelength division multiplexing*. Nevertheless, the main disadvantage of this process is the complexity and related costs of inscribing the fiber with different FBG and the limited number of gratings that can be interrogated for a given source of bandwidth (After Appel et al, 2007).

In addition to *wavelength division multiplexing* process, the *Optical Time Domain Reflectometry* (OTDR), can be applied and basically define the arrival time of the reflected signal and enable interrogation of very long fibers, but is limited to a special resolution between adjacent gratings. Another alternative is the *Optical Frequency Domain Reflectometry* (OFDR), which enable simultaneous sampling thousands of FBG written at spacing as close as 1 cm. Figure 11 shows an example of multiple FBG signals interpreted from the OFDR process.

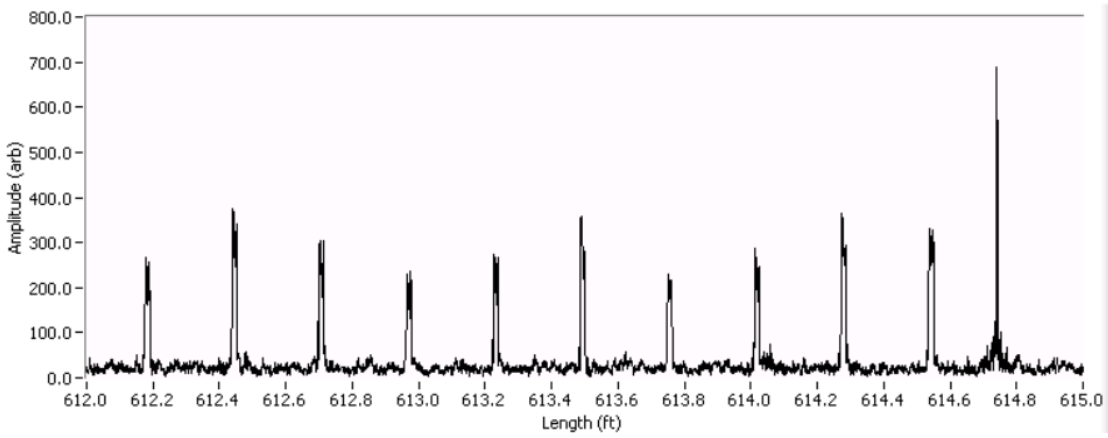

Figure 11: Example of light signals reflected on multiple FBG as function of length along the fiber and processed from OFDR (after Appel et al, 2007).

After understanding how the signals of FBG are processed and analyzed, it is important to point out how this FBG can be part of an integrated system. This is the case of the Real Time Compaction Imager (RTCI), which is a monitoring system comprised of three key elements: a tubular instrumented with an optical fiber cable, a surface interrogation unit (SIU) and a computer as illustrated in Figure 12.

The optical fiber in the RTCI system is the passive sensing element that contains thousands of FBGs, which are essentially strain gauges distributed along its length. The fiber is wrapped around the well tubular at a determined wrap angle to monitor deformational changes. The SIU is used to probe the gauges on the fiber and acquire the resulting data. The computer is responsible for controlling the SIU, transforming the acquired data into strain measurements, and reconstructing an image of the well tubular. Both are located at the surface and are connected to the instrumented tubular via a fiber-optic lead-in cable as shown in Figure 12.

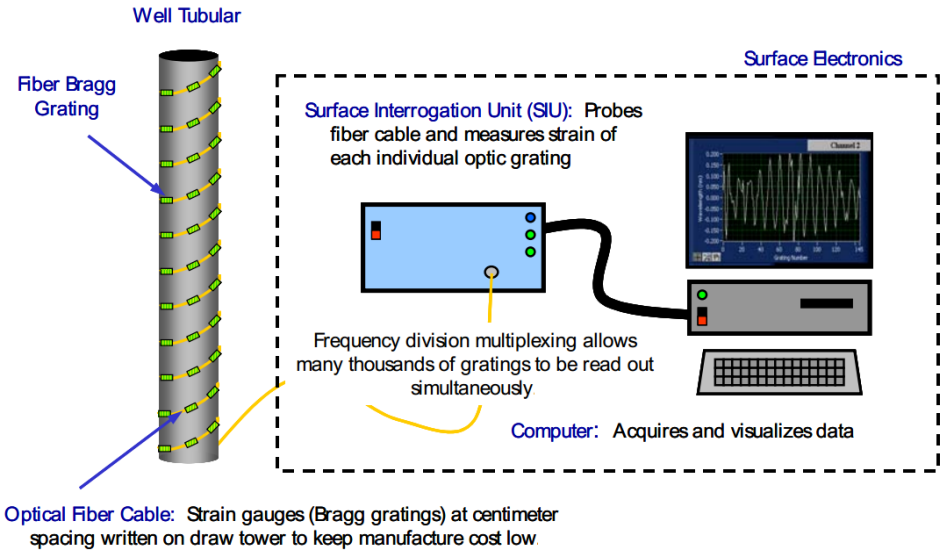

Figure 12: Components of the Real Time Compaction Imager (after Pearce et al, 2009).

Due to the optical fiber helically wrapped around a well tubular at a fixed angle, different deformation modes can be distinguished from the RTCI system, including: *axial compression* (compression of the axis of the tubular which result in a decrease in the axial length and increase of the tubular diameter), *bending* (a change in curvature of the tubular), *ovalization* (the lengthening of one radial direction and shortening of the orthogonal radial direction), *pressure* (radial expansion of the diameter caused by an increase of differential pressure) and *temperature* (cause an expansion of the surface area of the tubular). Figure 13 shows the typical deformational modes due to various well tubular deformations.

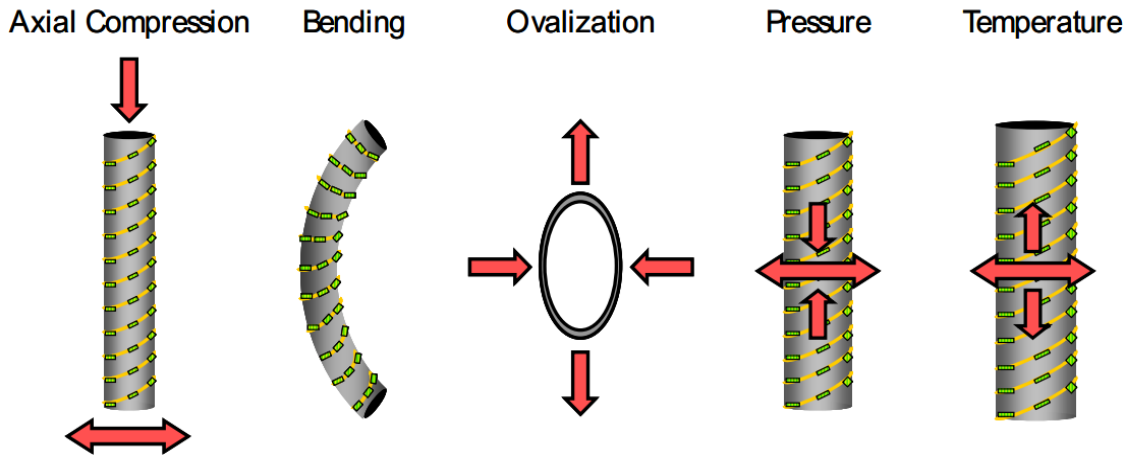

Figure 13: Typical deformational modes processed by RTCI system (after Pearce et al, 2009).

The strain along the fiber due to different deformation modes can be calculated as follows:

$$\varepsilon_f = -1 + (1 + \alpha\Delta T)\left[sin^2\theta(1+\varepsilon_c)^2\left(1-\upsilon\varepsilon_o(\phi_n)\right)^2\left(1+\varepsilon_b(\phi_n)\right)^2\left(1-\upsilon\varepsilon_p\right)^2 + cos^2\theta(1-\upsilon\varepsilon_c)^2\left(1+\varepsilon_o(\phi_n)\right)^2\left(1-\upsilon\varepsilon_b(\phi_n)\right)^2\left(1+\varepsilon_p\right)^2\right]^{1/2} \quad \textit{Eq. 10}$$

where α is the linear thermal expansion coefficient of the tubular, ΔT is the change of temperature, θ is the wrap angle, and υ is the Poisson's ratio of the material. The parameters ε_c, ε_o, ε_b, ε_p are the respective strains on the tubular due to axial compression, ovalization, bending and pressure. The bending and ovalization strains depend on ϕ_n, the azimuthal location of grating n. The pressure strain ε_p is essentially the hoop strain of a tubular due to the differential pressure or stress across the wall (Royalance, 2001):

$$\varepsilon_p = \frac{\Delta P_d r_i}{Et} \quad \textit{Eq. 11}$$

where ΔP_d is the change in differential pressure, r_i is the internal radius of the tubular, E is the Young's modulus of the material and t is the wall thickness.

Figure 14 presents the fiber strain for different tubular deformation modes as a function of the azimuthal angle around the tubular processed by the RTCI system.

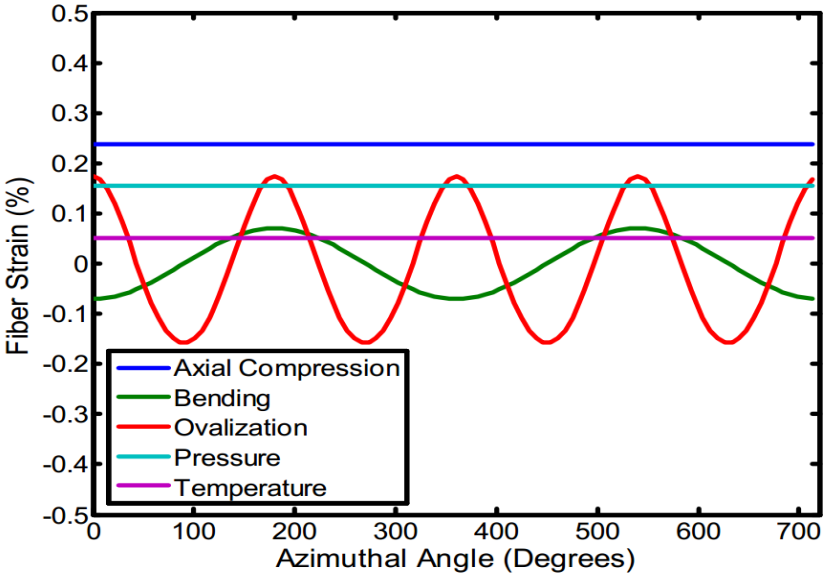

Figure 14: Fiber strain for different well tubular deformations versus its location (azimuthal angle) around the tubular processed by the RTCI system (after Pearce et al, 2009).

4.1.2 Distributed Fiber Optic Sensing

As discussed in the previous approach, FBG sensors are discrete sensors that allow strain measurements only in a limited number of points, which represent its main disadvantage. However, distributed Brillouin Scattering Time Domain Reflectometry (BOTDR) sensors are intrinsically capable of performing strain measurements in several hundreds or thousands of measuring points simultaneously along the fiber itself fiber by attaching a BOTDR analyzer to one end as presented in Figure 15. The novel aspect of this technology lies in the fact that tens of kilometers of fiber can be sensed at once for continuous distributed strain measurement, providing relatively cheap but highly effective monitoring systems. The system utilizes standard low cost fiber optics and the strain resolution can go down to 2 micro strains (Soga et al, 2008).

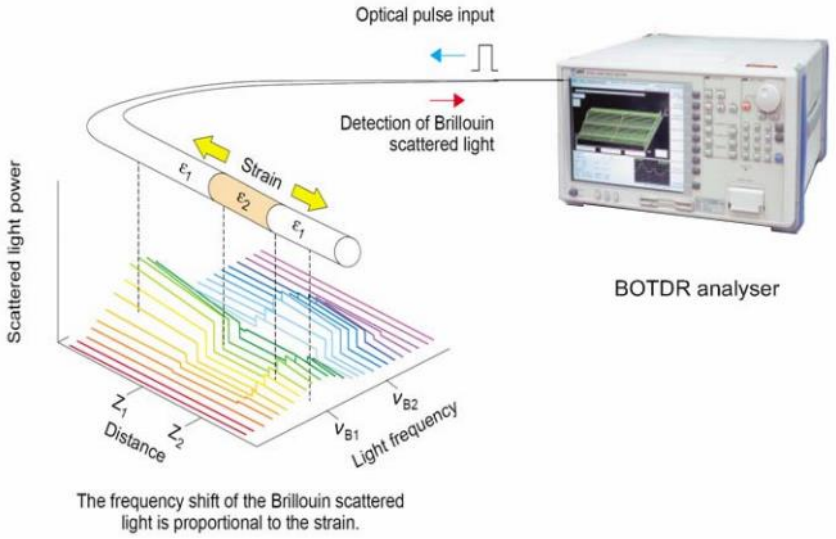

Figure 15: BOTDR Analyzer (after Soga et al, 2008).

As referred previously in Figure 8, when a pulse of light travels down an optical fiber, the majority of light travels through but a small fraction is scattered back at every location along the fiber. The frequency of this back scattered light is shifted from the original input frequency by an amount linearly proportional to the temperature and strain applied at the scattering location. The Brillouin Frequency Shift (BFS) is expressed by the following relation (Minardo et al, 2015):

$$\upsilon_B = 2\frac{nV_a}{\lambda_0} \qquad \textit{Eq. 12}$$

where n is the effective refractive index of the fiber, V_a is the acoustic velocity, and λ_o is the optical wavelength. As the effective refractive index and the acoustic velocity vary with temperature and strain, the BFS has a linear dependence on temperature and strain over a wide range, so it can be written as (Minardo et al, 2015):

$$\Delta v_B(T, \varepsilon) = C_\varepsilon \Delta_\varepsilon + C_T \Delta T \qquad Eq.\ 13$$

where C_ε is the strain coefficient and C_T is the temperature coefficient. These coefficients are mostly determined by the fiber compositions, pump wavelength, fiber coatings, and jackets.

For casing deformation and strain monitoring, some of the most typical distributed fiber optic sensing include Distributed Strain Sensing (DSS) and simultaneous Distributed Temperature and Strain Sensing (DTSS) technologies, which consider the Brillouin Frequency Shift.

DSS allows monitoring tiny well deformations during the lifetime of a well. By helically wrapping the optical fiber around casing, sand screen or well tubular, three-dimensional images of well deformation at a centimeter spatial resolution can be obtained. This data can be used to detect well deformation trends and to prevent future well failure. In addition, information about reservoir geomechanics response to production or injection can be performed. It is important to highlight that DSS data should be acquired in combination with DTS data, such that the measured strains can be decomposed into mechanically and thermally induced strains (Koelman et al, 2012).

An example of DSS and DTS can be seen in Figure 16. Note that the 2D strain image on the top indicates strains ranging from -0.03% to +0.03% corresponding to micrometer deformations over centimeter length scales. It was installed together with the data from DTS fibers along four azimuthal positions. Also, the DTS system responds to thermal effect only, while the DSS system is sensitive to both mechanical and thermal strain and yields data at a much higher spatial resolution.

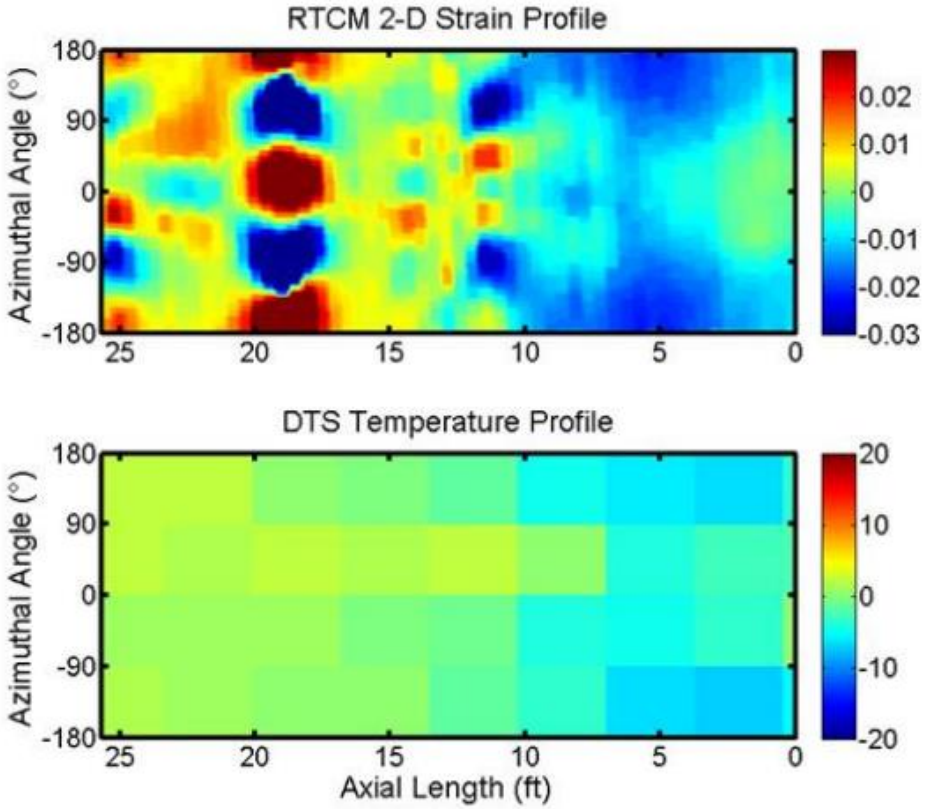

Figure 16: DSS and DTS measurements (after Koelman et al, 2012).

4.2 Borehole ultrasonic tools

It is well known that typical casing inspection logging tools such as calipers, phase-shift tools, and flux-leakage devices often have been unable to function mechanically in larger size casing. Additionally, small pipe defects can go unnoticed due to poor azimuthal resolution of the measurements or to the averaging techniques, in both casing and risers, using previous casing inspection methods. However, ultrasonic devices can provide precise casing inspection for most casing sizes. The use of a navigation package permits data to be corrected for orientation and tool rotation. Data such as casing inner diameter and radius, casing ovality, and 40 to 200 caliper traces may be recorded in real time in conventional or imaging log formats, permit monitoring over time (Frisch G. and Mandal B, 2001).

These ultrasonic tools acoustically scan the circumference of the wellbore or casing to furnish improved images. Improved tool design, telemetry, and waveform analysis provide remarkable borehole and casing inspection and cement evaluation capabilities.

The ultra-sonic imaging tool uses two ultrasonic transducers. The primary transducer is mounted in a rotating scanner head that transmits ultrasonic signals and receives reflections from the casing or formation. The secondary transducer is secured in a fixed

position with the signals reflecting from a flat target plate and provides data concerning the wellbore fluid travel time. High-density fluids rapidly attenuate ultrasonic signals and reduce the amplitude of waveforms received. (Frisch G. and Mandal B, 2001).

This tool can operate in either image mode or cased hole mode. In the "cased hole mode", data is acquired from the interior diameter of the casing, the casing thickness, and the annular space between the casing OD and surrounding formation. In "image mode", the tool acquires data from the interior diameter of the pipe or formation. The ultrasonic scanner operates in cased hole mode when a thorough casing assessment (including wall thickness) is needed or when pipe-to-cement evaluation is needed. The cased hole mode determines both the internal radii of the casing and the casing thickness.

In image mode, the scanner evaluates only the "inner" surface of the target (the formation bounding the wellbore or the inner wall of the casing). This mode provides both visual and digital data to indicate casing integrity or problems. These images are useful for evaluating casing integrity by revealing distortion, wear, holes, parting, and other anomalies on the inner wall of the casing.

Regarding the interpretation, the data from the ultrasonic tool is usually presented in an image format corrected for wellbore orientation with the low side of the hole displayed in the middle of the track. Images are used to evaluate casing integrity by revealing distortion, wear, holes, parting, and other anomalies of the casing. In the image mode of tool operation, travel time and amplitude are usually presented as images ranging from white to black. Low amplitude and longer travel times are shown in darker colors while higher amplitude and slower travel times are presented with lighter colors. These color pallets allow a visual representation of the examined surface. Usually the amplitude image shows more detail than the travel time image due to the waveform characteristics. Figure 17 shows an example of 2D image amplitude and 3D image along with the amplitude and corrected travel time.

The cased hole images are normally color coded for ease of interpretation. In all of the examples, red indicates a decrease in the nominal casing thickness, either due to an increase in the internal diameter or reduction in casing thickness. Blue indicates an increase in the nominal casing thickness, due to a decrease in the internal diameter or increase in casing thickness (Frisch G. and Mandal B, 2001). Figure 18 presents an example of a deformed casing showing the ovality (first track on the left), casing radius and thickness maps.

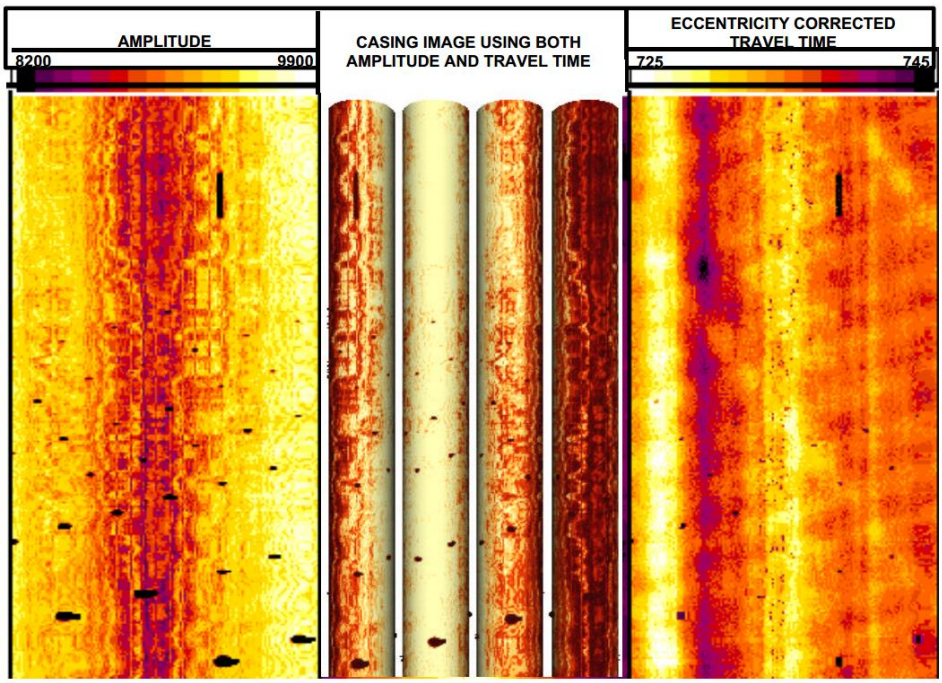

Figure 17: Borehole ultrasonic example for a 2D image amplitude, 3D image along with the amplitude and corrected travel time (after Frisch G. and Mandal B, 2001).

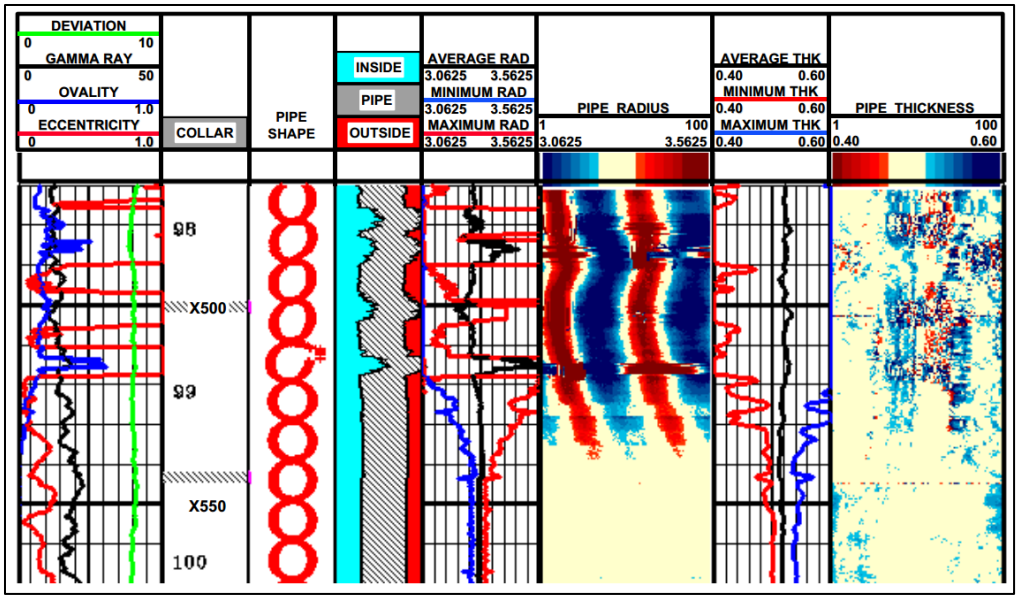

Figure 18: Example of a deformed casing showing the ovality (first track on the left), casing radius and thickness maps (after Frisch G. and Mandal B, 2001).

Multifinger Imaging Tool (MIT) is another example of a borehole ultrasonic tool. A wide variety of multi-arm calipers can provide high resolution details about the condition of the casing or tubing, including accurate measurements of its internal radius. The MIT tool

is available for most casing and tubing sizes. The tool can operate 24 to 60 arms and is deployed on wireline, slick line, or coiled tubing (Halliburton Services, 2017).

The 60 finger MIT is used to detect very small changes to the internal surface condition of tubing or casing with a high grade of accuracy. The number of fingers increases with the diameter of the tool to maintain maximum surface coverage. When the tool is run in hole, the fingers are closer to prevent damage. Once at logging depth, a motor is activated from the logging system or by the memory tool and the fingers open. The tool has an inclinometer to indicate the finger positions relative to the high side of the pipe, so that features can be oriented correctly during data processing. Figure 19 shows an example of MIT with 60 fingers (Liu H., 2017). All data collected is used to generate 3D images of the casing or tubing as seen in Figure 20 (Halliburton Services, 2017).

Figure 19: MIT-60 Multifinger Imaging Tool (after Liu H., 2017).

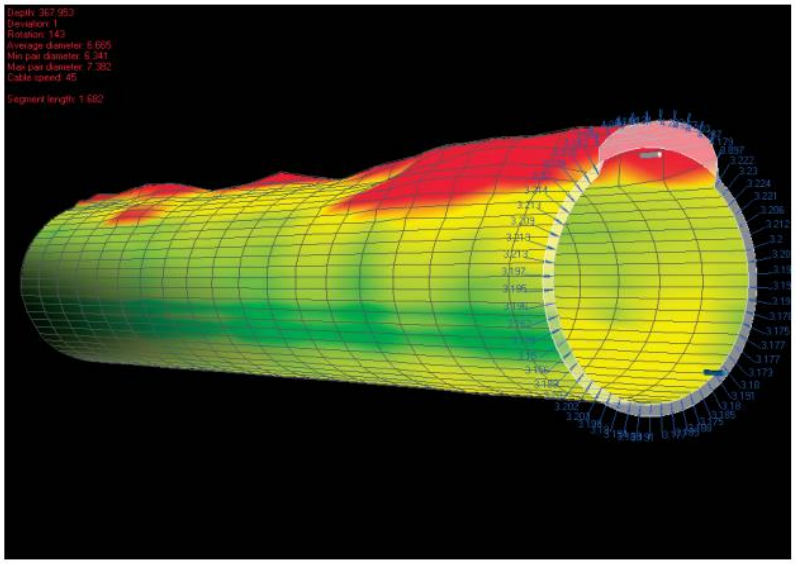

Figure 20: Casing deformation image interpreted from a Multifinger Imaging Tool (after Halliburton Services, 2017).

4.3 Electromagnetic tools

Electromagnetic instruments can be also used for evaluation of wellbore casing conditions, like corrosion or deformation. This type of devices is utilizing mainly two various physical principles (Brill, T.M., et al., 2012; Castaneda, C., et al., 2014):

- Remote-Field Eddy-Current (RFEC) tools, which measure the response of the transmitted electromagnetic (EM) field, – these tools uses RFEC ND technique. They are measuring the total EM thickness of the casing and detect large-scale and generalized metal loss
- Flux leakage tools, which measure magnetic flux anomalies, – designed to detect localized casing defects as corrosion patches, pits and holes. The tool measures local magnetic flux anomalies caused by casing wall irregularities, using pad-mounted sensors.

The main purpose of RFEC techniques is to determine corrosion locations in casing by measuring the total metal thickness and metal loss. A new slim electromagnetic imaging tool stimulates eddy-currents by using a low-frequency solenoidal transmitter in the tubulars. The measurement directly determines the total metal thickness and localizes the metal loss on the image (Brill, T.M., et al., 2012).

Another type of tool, which uses the same physical principle, is the new Electromagnetic Scanning Tool. It is smaller than RFEC and it is able to get the azimuthal data in addition. Another advantage of this instrument is that it can pass through the tubing. The device carries out three types of measurements (Castaneda, C., et al., 2014):

- Mandrel measurement, which assesses the metal thickness at low frequency and large coil separations by analyzing the change of the waves propagation through the casings
- Z-property measurement, which is conducted at high frequencies (>500Hz) to get the surface impedance of the casing, casing magnetic permeability and electrical conductivity. These parameters are used to correct the results for inner diameter and wall thickness. Magnetic permeability volatility can indicate the mechanical stress or heat exposure of the casing.
- Imaging section, which uses 18 radially distributed pads containing miniature magnetic coil sensors and provide a radial image. It detects a defect on inner side of the casing.

The tools described above are used to analyze the corrosion or to detect an already existing hole or discontinuity in the pipe, therefore they are well suited for obtaining the casing integrity. However, the casing measurements done with these tools do not allow monitoring the stress or strain, which would be of interest in this study.

The group of devices that uses the magnetic flux leakage seems to be more useful for the project objectives. The tools designed for detecting a magnetic flux leakage can measure

or predict a casing strain. In these devices, a Magnetic Memory Method (MMM) is used. It is a non-destructive diagnostic technique, which was first presented by Dubov in 1997. This technique utilizes a self-magnetic flux leakage (SMFL) of a ferromagnetic material. Due to the Earth's magnetic field and an external loading acting on a ferromagnetic material, a stress concentration zone (SC) occurs. Dubov invented a technique, which allows to detect the stress concentration zone by analyzing the distribution of the components of magnetic flux leakage at the surface of material. The normal component Hp(y) of this magnetic scattering field changes its polarity (has a 0 value) in the place of the material inhomogeneity, while the tangential component Hp(x) reaches its maximum value in such a location. This method allows one to detect a potential future source and location of the strain. Figure 21 presents curves shape of the SMFL at the stress concentration zone. The characteristic magnetic signal at the material surface is observed even after loading is removed (Bao., S., et al., 2016).

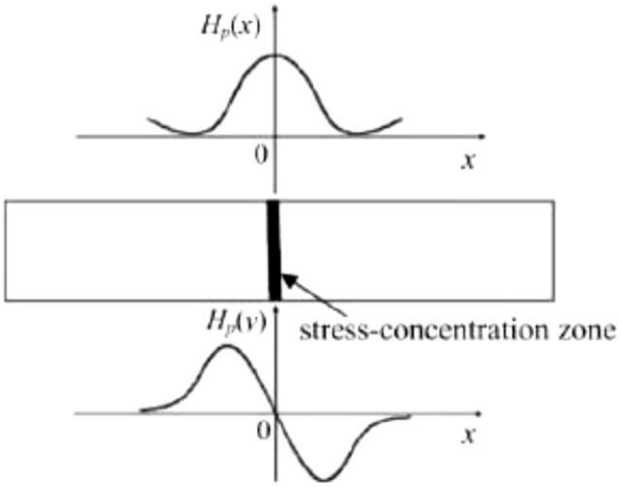

Figure 21: Schematic of self-magnetic flux leakage (SMFL) distribution in the stress concentration zone (after Bao., S., et al., 2016).

The most important advantage of the MMM is that it can diagnose an early defect or forecast a future crack in steel by detecting stress concentration zones. This method uses a natural magnetic field of the Earth, instead of an artificial magnetization source (Bao., S., et al., 2016; Sun, B., et al., 2014).

An example of the MMM application in the oil well casing was the field test of magnetic memory sensor in the Daqing oilfield. A few types of magneto sensors can detect a weak natural magnetic field: HALL, Anisotropic magneto-resistance AMR, Giant magneto-resistance GMR. Among the listed instruments, a GMR was chosen as the best tool meeting all the requirements of downhole conditions, which are: wide range of detection magnetic field, small size, high temperature sensitivity and its tolerance as well as insulation and isolation. Table 1 presents a comparison of the three different types of tools mentioned earlier. Figure 22 shows the diagram of the circuit assembly (Sun, B., et al., 2014).

Table 1: Comparison of magneto sensors (after Sun, B., et al., 2014)

	Magneto sensor		
Characters	Hall element	AMR	GMR
Detection principle	Hall effect	Magnetoresistance effect	Giant magnetoresistance
Detection range (Gs)	0.1-1000	10^{-6}-10	10^{-6}-106
Sensitivity	7μ V/V/Gs	0.8-4 mV/ V/Gs	0.3-18 mV/ V/Gs
Frequency response range	0-100 KHz	0-5 MHz	0-1 MHz
Temperature stability	Low	Medium	High
Detective circuits	Temperature-compensation	Set/reset circuits	Simple

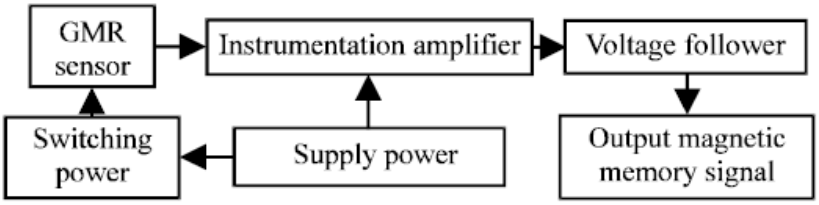

Figure 22: Circuit diagram (after Sun, B., et al., 2014)

The GMR sensor was used together with an amplifier in order to filter and strengthen the output signal. Also, an extra voltage follower with isolation and buffer were added. The magneto sensor was fixed, sealed and insulated for the stability in the downhole conditions. For the field tests, which were carried out in the new perforated casing well, a set of 18-arms lantern casing damage detector was developed. The recorded data from the target logging horizon were filtered with the wavelet method. The result in Figure 23 shows the signal amplitude changes in the perforated holes. This proved that the designed tool could be used for the evaluation of the early detection of casing damages (Sun, B., et al., 2014).

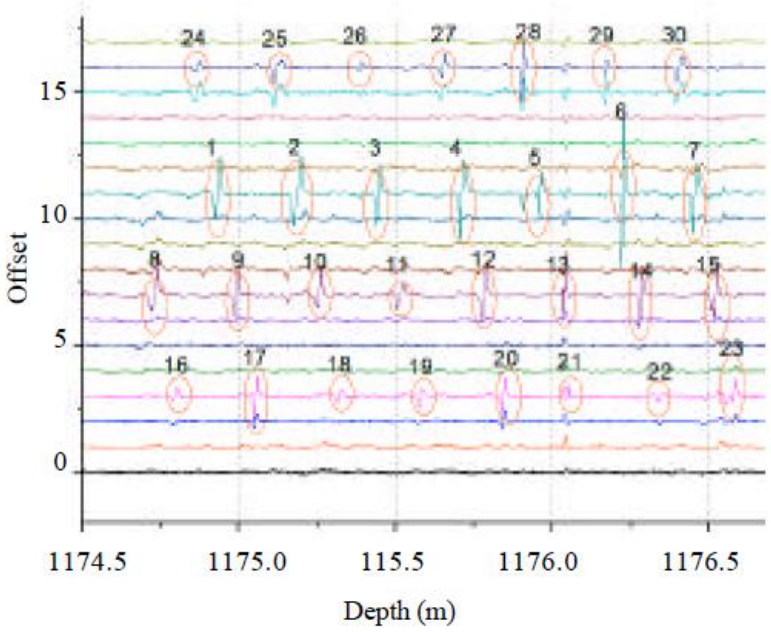

Figure 23: Color waterfall plot graphic (after Sun, B., et al., 2014)

An another example of utilising the MMM presents the analyses of magnetic field curves distribution and their convertion for evaluation of the casing stress distribution. This approach can be used to predict the risk of casing damage. An experimental model machine of metal magnetic memory inspection (MMI) which was developed by Daqing Logging & Testing Services Company (DLTS) together with EDDYSUN Company (Xiamen). Based on the laboratory test of 25 downhole casing pieces of the same size, a peak-to-peak changes of magnetic memory response curves were analyzed and a four-class semi-quantitative evaluation method was derived for evaluating the risk class of potential casing damage. Another test was carried out in the field. Figure 24 shows the curves recorded by the downhole casing stress MMI model machine tested in one of the wells. Locations of the strong curves peaks identifies a casing collars. At the depth of 307 m curves change their polarity. Also a peak-to-peak appears arround zero point, hence this can indicate that this is a location of the stress concentration zone (Liu, Q., et al., 2008).

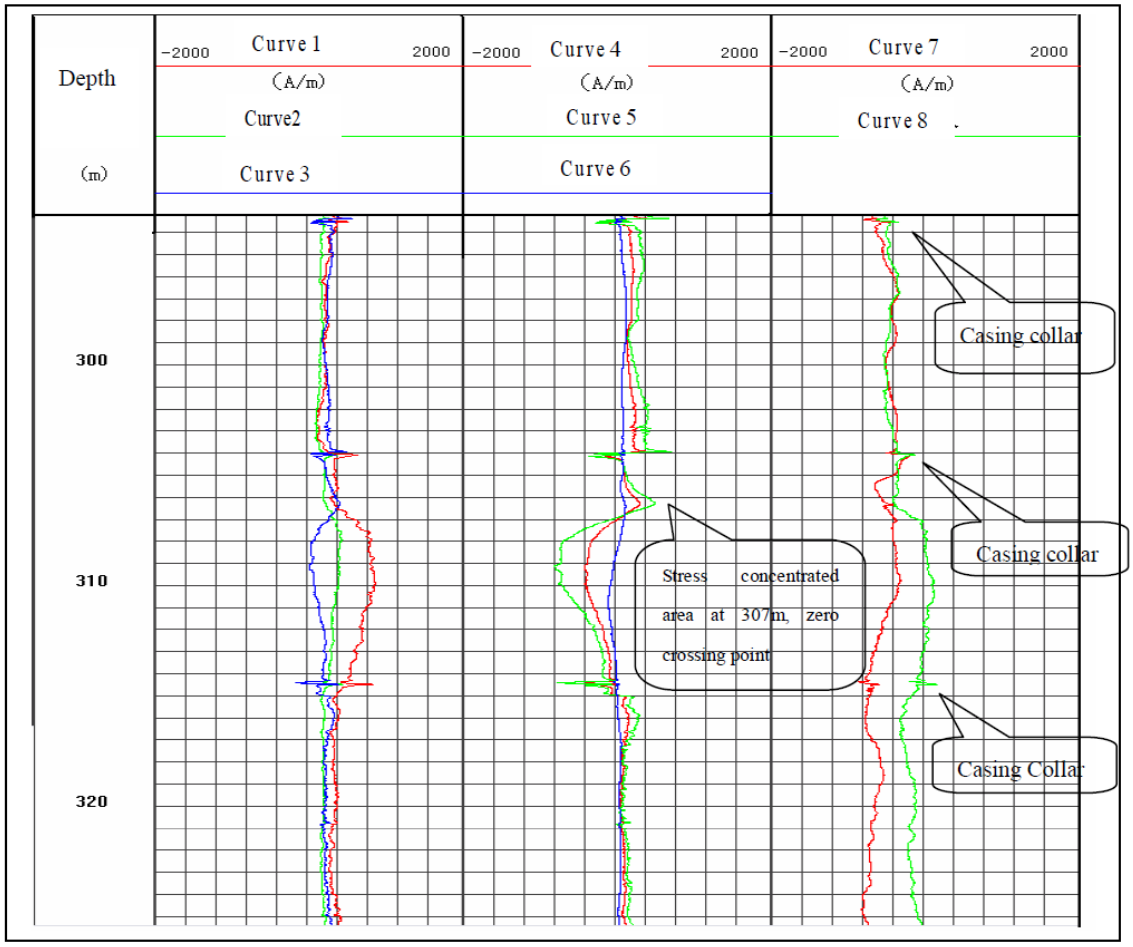

Figure 24: Field Experiment curves of Casing Stress MMI in Well-L15B264 (after Liu, Q., et al., 2008).

5. Numerical Model Development and Documentation (Task 4)

A 3D geomechanics model was assembled using the numerical modeling software Flac3D with a volume covering 65.6 ft (20 m) by 32.8 ft (10 m) by 32.8 ft (10 m), as shown in Figure 25. The model was set up at depth of 9842 ft (3000 m) and three stratigraphy layers were assumed for the conceptual model. The top of the model contains a caprock layer that is 13.12 ft (4 m) thick, followed by a small Reservoir layer that is 6.56 ft (2 m) thick, and a Basement layer at the bottom that is 13.12 ft (4 m) thick. A hydraulic fracture was set up in the middle of the model and a casing and cement interface along the x-axis to represent a horizontal wellbore. A fracture length of 19.6 ft (6 m) and height of 6.5 ft (2 m) were assumed.

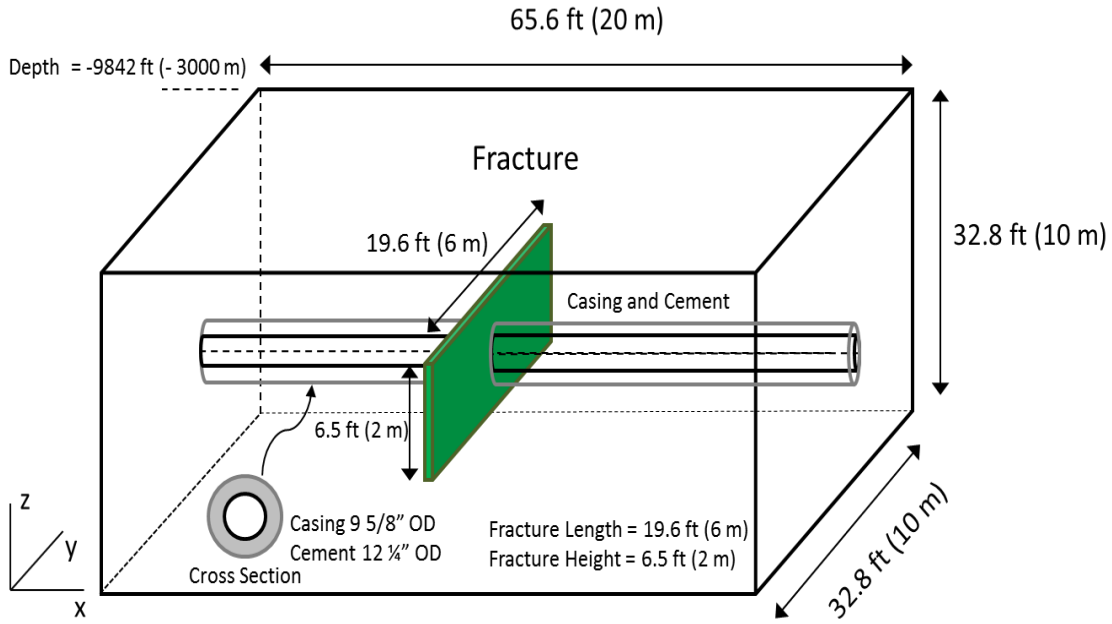

Figure 25: Conceptual model without casing and cement interfaces.

To evaluate the induced strains along the wellbore, a variation in fracture orientations were performed every 10 degrees from the horizontal wellbore as presented in Figure 26. Due to model symmetry, the right section of the horizontal wellbore was only considered for monitoring the induced axial strain from the center of the fracture to the right end of the horizontal well at 10 m. In addition, three locations around the wellbore were defined to monitor the induced axial strain between casing, cement and reservoir interfaces as seen in Figure 27.

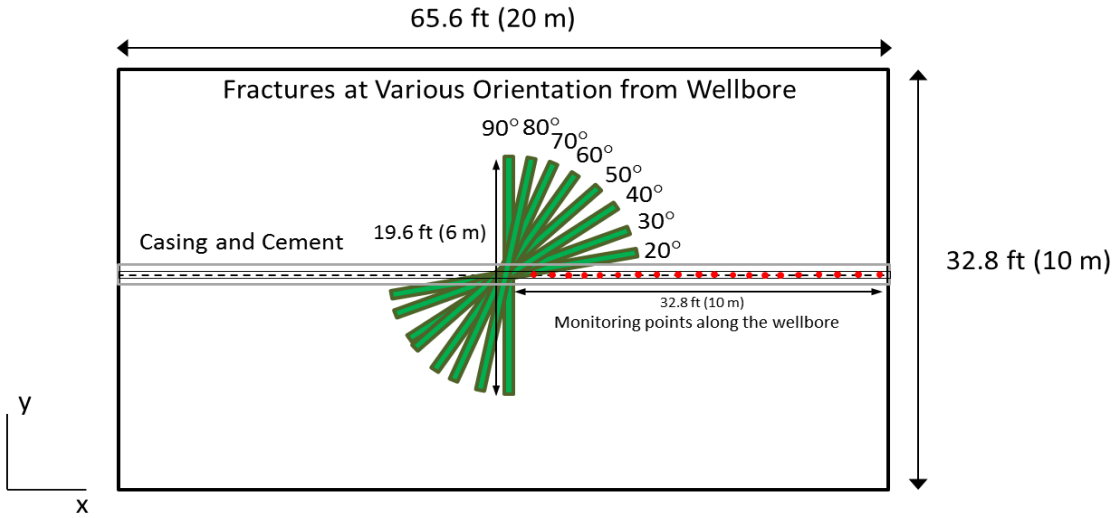

Figure 26: Variation in hydraulic fracture orientation with respect to the horizontal wellbore with casing and cement interfaces.

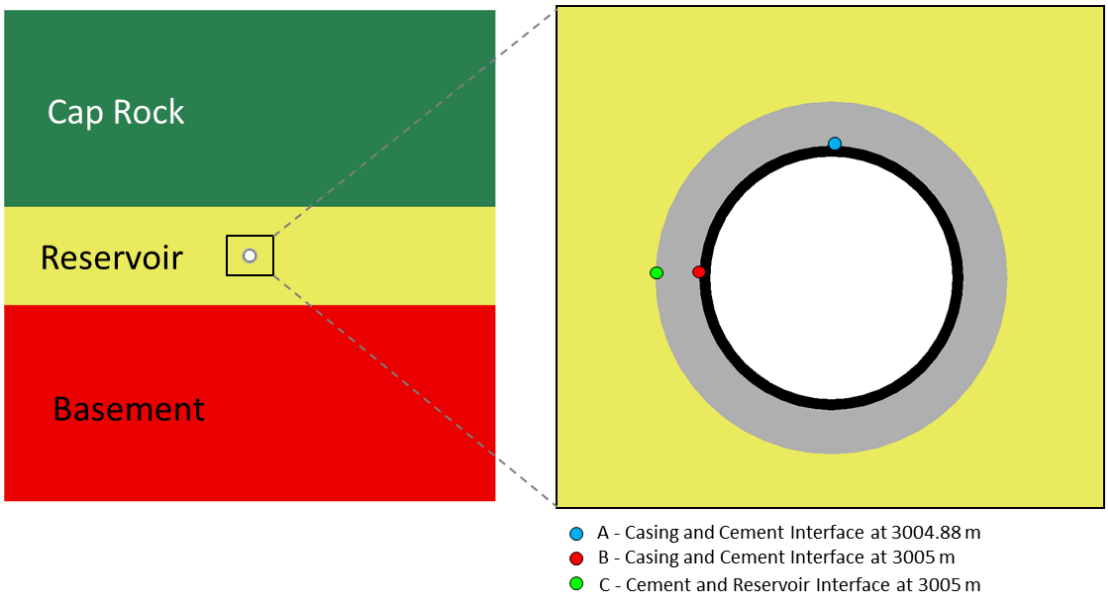

Figure 27: Monitoring point locations around a wellbore cross section considering casing, cement and reservoir interfaces.

Table 2 summarizes the mechanical properties assumed for all materials considered in the conceptual model. Note that the cement is a weaker material compared to the casing and reservoir materials.

Table 2: Mechanical properties for conceptual model

Material	Young Modulus	Poisson's ratio	Tenslie Strength	Cohesion	Friction Angle
	Pa	unitless	Pa	Pa	Degree
Caprock	40e9	0.3	-	-	-
Reservoir	20e9	0.25	-	-	-
Basement	40e9	0.3	-	-	-
Fracture Zone	20e9	0.25	0	3e6	25
Casing Steel L-80	20.6e12	0.25	-	2.75e8	0
Cement	1.82e9	0.28	1.37e6	2.87e6	4

A mesh was developed with a higher resolution around the vicinity of the casing and cement (Figure 28). A total number of 545,440 elements were defined and we applied a roller boundary condition along the *x, y* and *z* bottom directions, and free movement at

the top of the model. Induced axial strain was estimated after applying a pressure equivalent to 6.895e6 pa (1000 psi) along the fracture plane. Figure 29 is a top view of the hydraulic fractures at different orientations from the horizontal wellbore at every 10-degree increment.

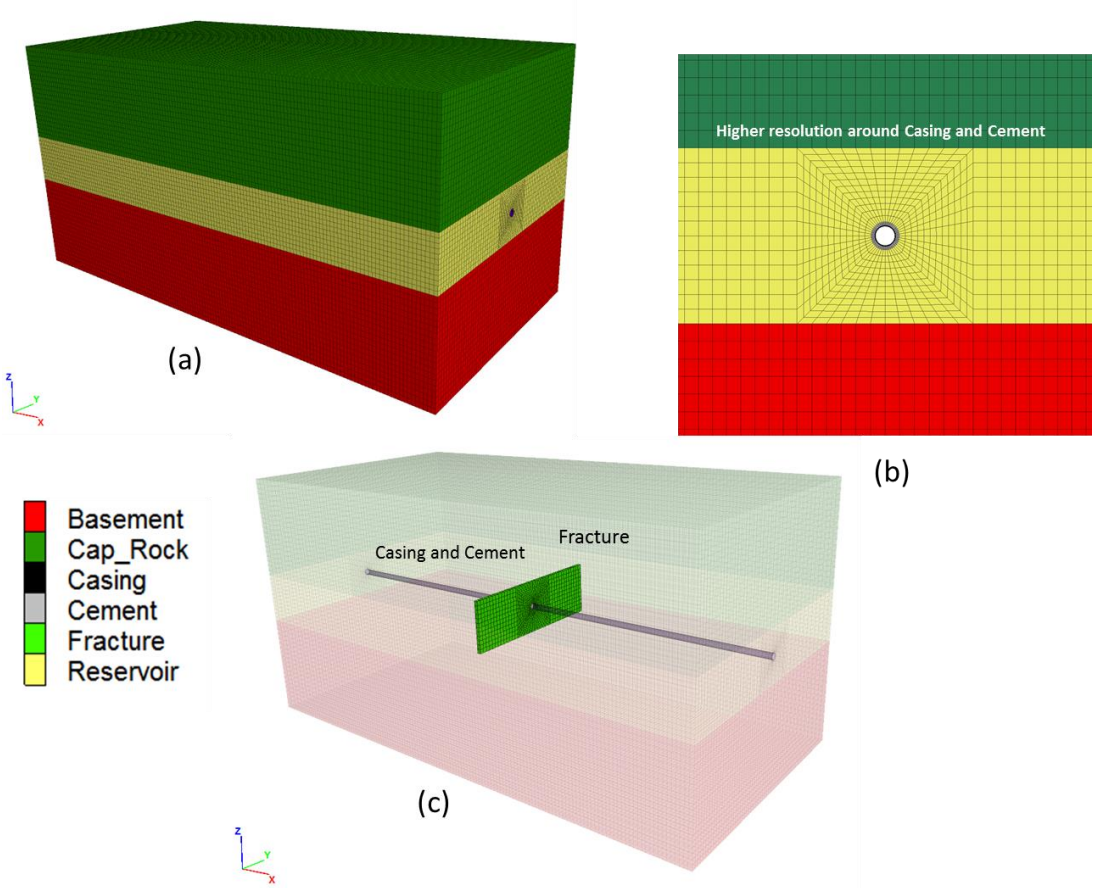

Figure 28: 3D conceptual model mesh (a), cross section showing higher resolution around casing and cement (b) and 3D transparency conceptual model showing casing, cement, and fracture (c).

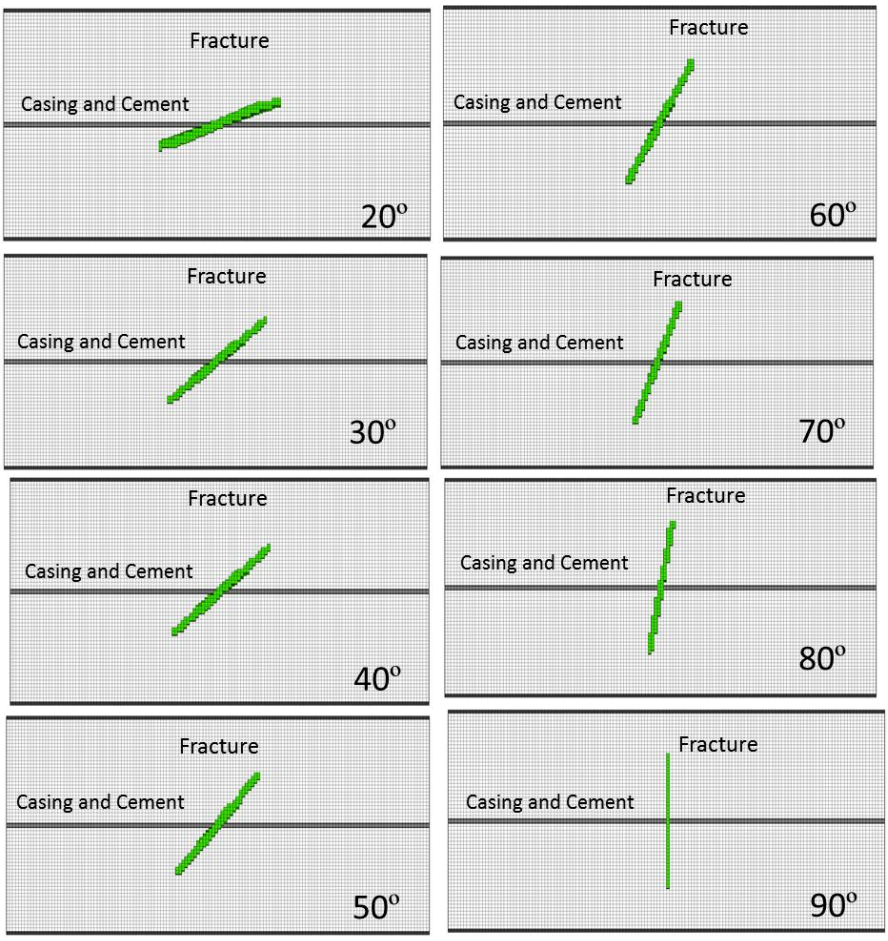

Figure 29: Top view of hydraulic fractures oriented at different angles every 10 degrees, from 20 degrees to 90 degrees, with respect to the horizontal well casing and cement.

After applying the pressure change along the hydraulic fracture, induced axial strain were estimated for each orientation as presented in Figure 30. It is important to highlight that the axial strain is estimated by the induced displacement along each mesh element as a result of the pressure change along the fracture. Note that a positive axial strain increment value along the fracture is an indication of tension. As the angle increases from 20 degrees to 90 degrees, a higher strain increment of 6.06e-4 m (0.023 in) is obtained inside the fracture. Nevertheless, the negative induced axial strain increment imposed along the casing indicates compression. Also, it is clear that a more critical zone of induced strain along the casing is identified in the area near the middle of the fracture at angles lower than 30 degrees. This result is expected because the displacement imposed by the pressure change is higher as the fracture tends to be closer and more parallel to the horizontal well. Thus, overlapping and perturbation of strain patterns are expected in the critical zones at lower angles.

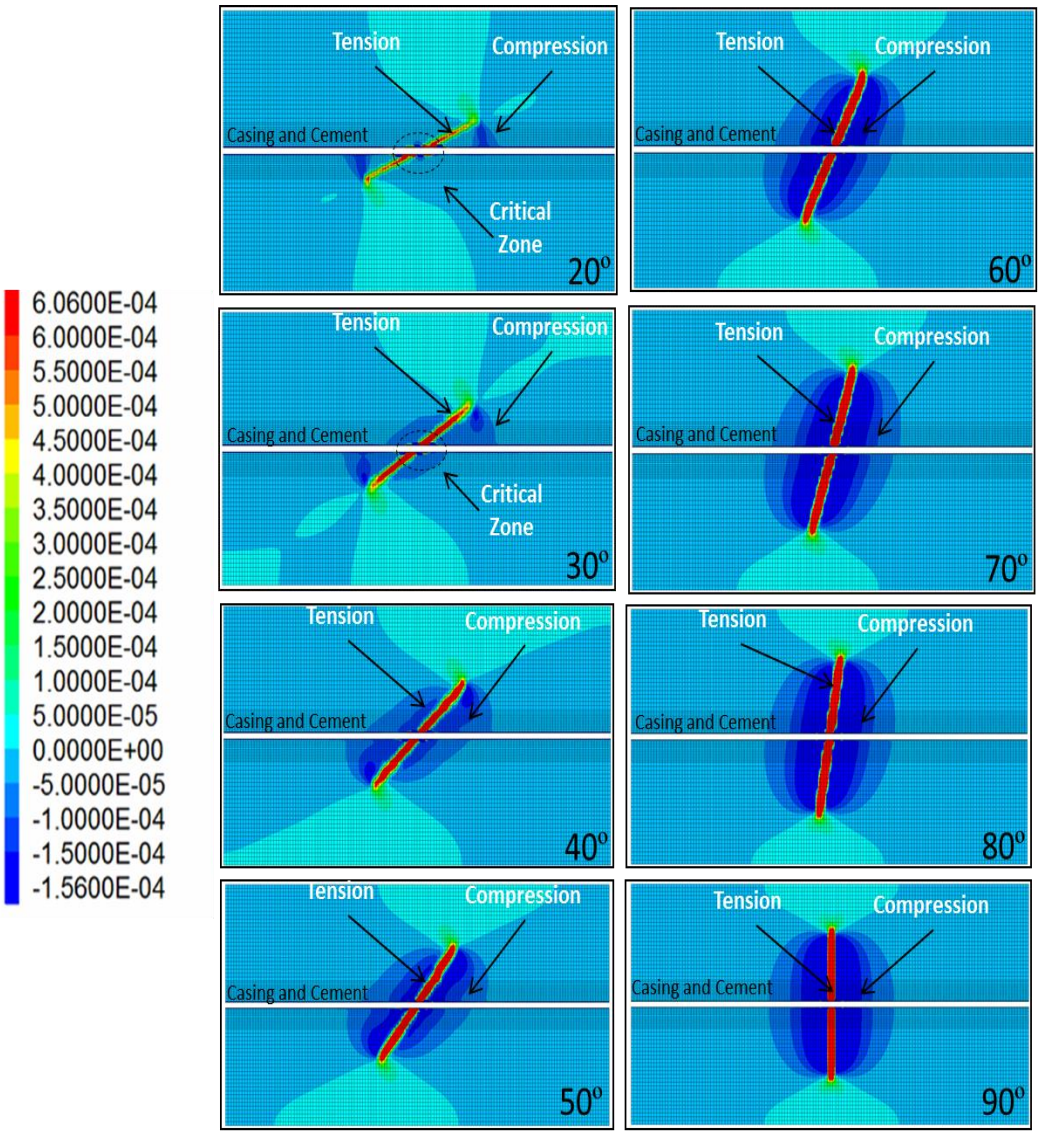

Figure 30: Top view of axial strain at different orientations varying by 10 degrees from 20 degrees to 90 degrees with respect to the horizontal well casing and cement.

Figure 30 shows an overall analysis of axial strain imposed along the casing. However, a more detailed result of axial strain not only along the horizontal wellbore but also around the casing, cement and reservoir interface locations (previously presented in Figure 27) are described in the next plots.

Figure 31 shows the axial strain along the wellbore including casing and cement interfaces at location "A". As seen, a critical zone with overlapping axial strain is estimated between 0.5 m (19.68 in) and 1.5 m (59 in). After that, a more clear and stable trend zone pattern is obtained for each orientation ranging from 20 degrees to 90 degrees. Figure 32 illustrates a zoomed in image with a more clear pattern for the stable zone. Note that a higher axial strain of around -0.00044 was obtained for angles below

20 degrees. Conversely, a lower strain (close to zero) was obtained for those cases ranging from 80 to 90 degrees.

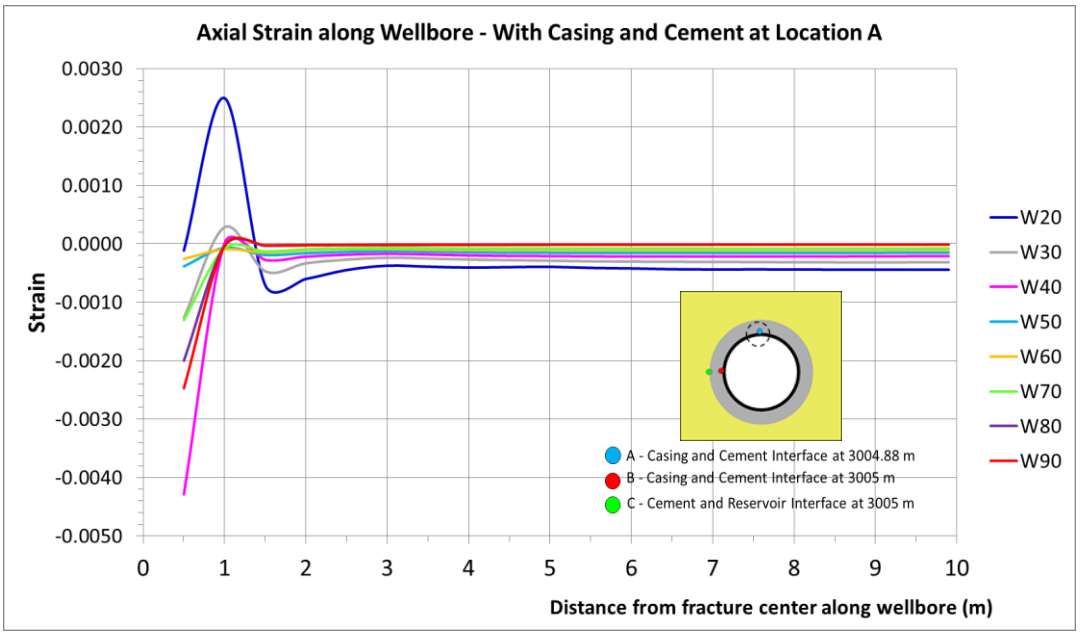

Figure 31: Axial strain curves along the wellbore including casing and cement interfaces at location "A".

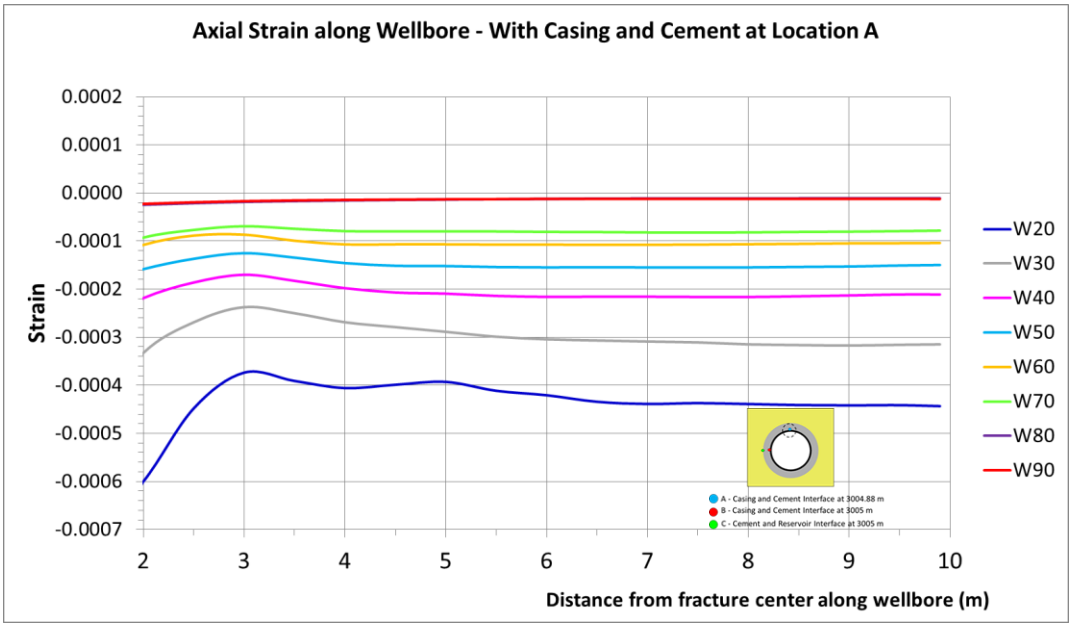

Figure 32: Zoomed in plot of axial strain curves along the wellbore including casing and cement interfaces for the stable zone at location "A".

A similar analysis was performed for location "B" and "C" as shown in Figure 33 to Figure 36.

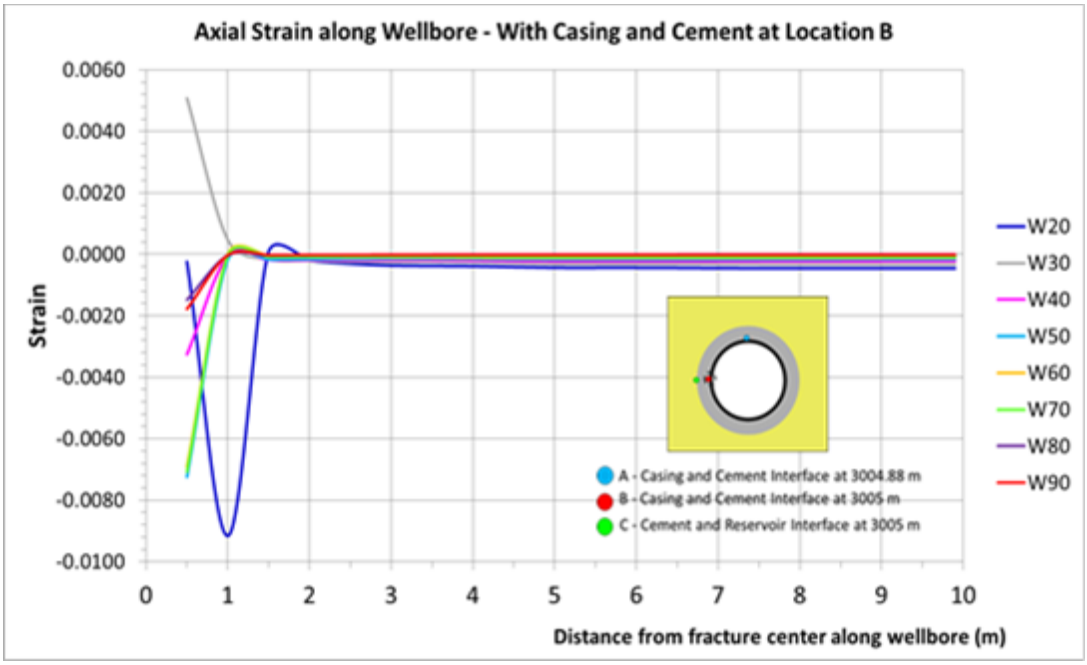

Figure 33: Axial strain curves along the wellbore including casing and cement interfaces at location "B".

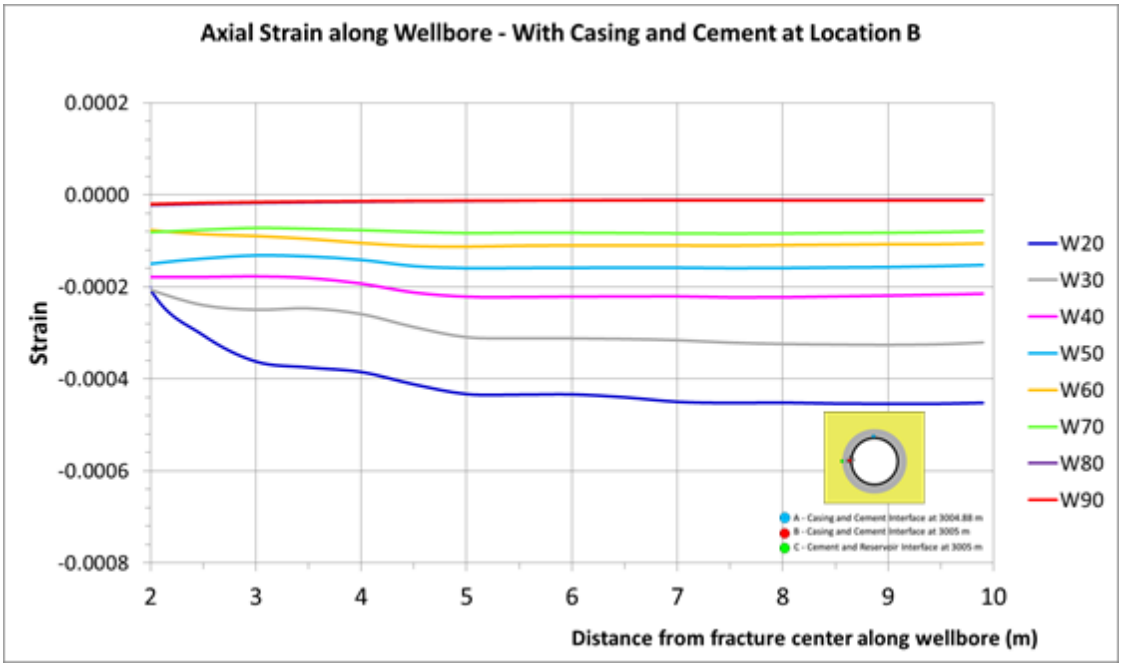

Figure 34: Zoomed in plot of axial strain curves along the wellbore including casing and cement interfaces for the stable zone at location "B".

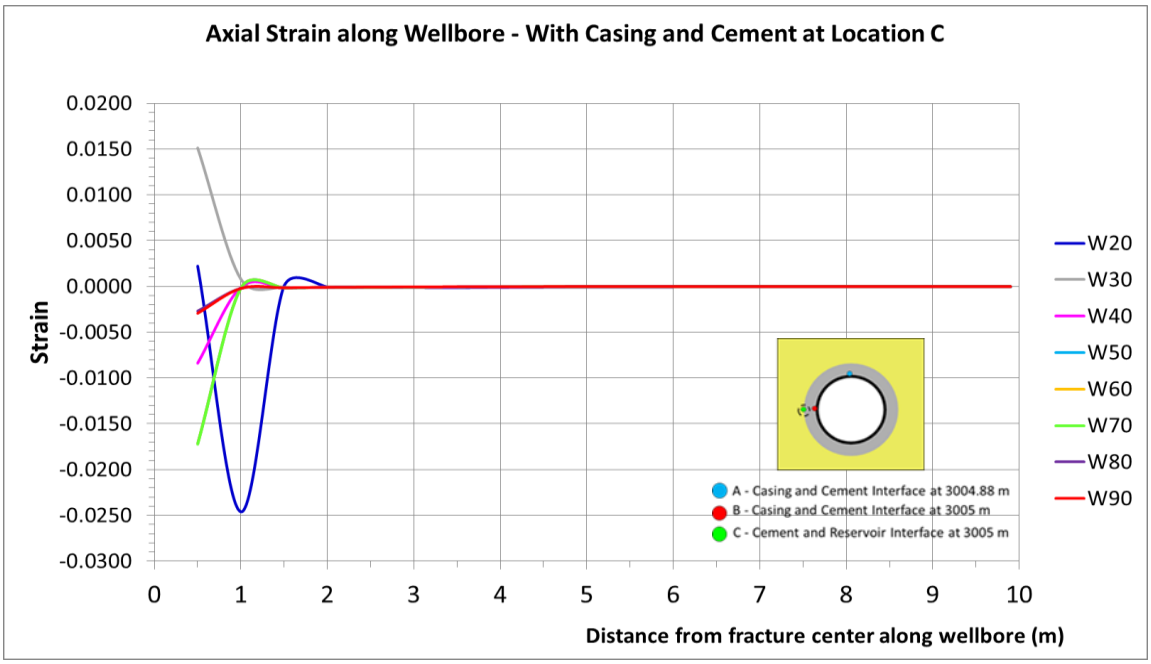

Figure 35: Axial strain curves along the wellbore including casing and cement interfaces at location "C".

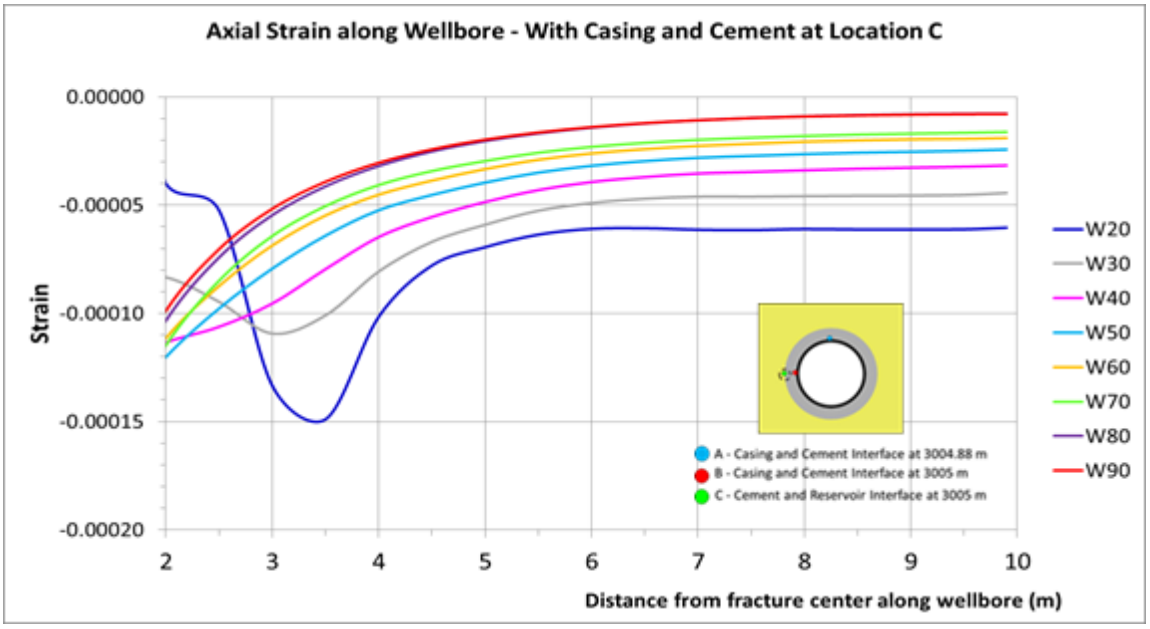

Figure 36: Zoomed in plot of axial strain curves along the wellbore including casing and cement interfaces for the stable zone at location "C".

As seen in Figure 33, a critical zone with axial strain overlapping is estimated between 0.5 m (19.68 in) and 2 m (78.74 in). After that, a more clear and stable trend zone pattern is obtained for each orientation ranging from 20 degrees to 90 degrees. Figure 34 shows a zoomed in plot with a more clear pattern for the stable zone. Note that a higher axial strain of around -0.00045 was obtained for angles below 20 degrees. Conversely, a lower strain (closed to zero) was obtained for the cases ranging from 80 to 90 degrees.

Regarding location "C", a longer critical zone with axial strain overlapping is estimated between 0.5 m (19.68 in) and 4 m (157.48 in) as seen in Figure 35. After that, a more clear and stable trend zone pattern is obtained for each orientation ranging from 20 degrees to 90 degrees. Figure 36 presents a zoomed in plot with a clearer pattern for the stable zone. Note that a higher axial strain of around -0.00006 was obtained for angles below 20 degrees. Conversely, a lower strain (closed to zero) was obtained for the cases ranging from 80 to 90 degrees.

Comparing all three locations, for example at an angle of 40 degrees, a significant difference can be noticed between the interface located at point "C" and those located at "A" and "B" as presented in Figure 37. The main reason is that there is a contrast of strength properties between the reservoir and cement as summarized in Table 2. Thus, a lower axial strain magnitude in the order of -0.000031 was estimated for location "C". However, similar results were obtained for location "A" and "B" because the interface casing and cement presents the same strength property conditions.

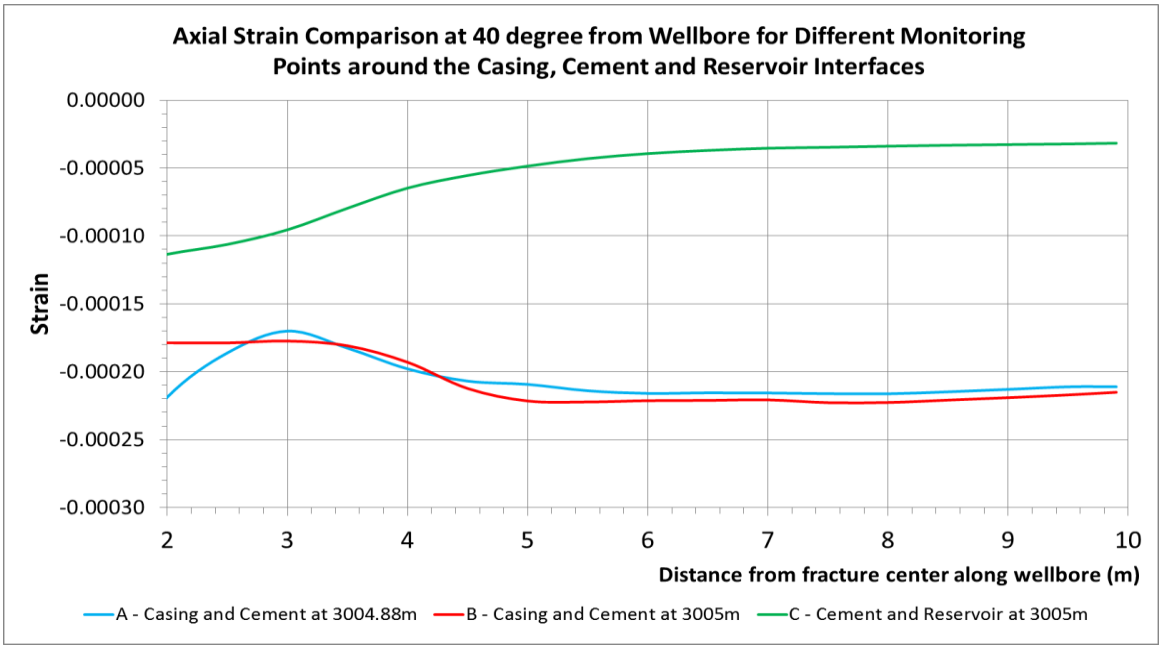

Figure 37: Axial strain comparison at 40 degrees from the wellbore for different monitoring point locations around the casing, cement and reservoir interfaces.

5.1 Inversion Technique

To predict the fracture orientation from an actual field data measurement, an inversion technique was applied to estimate the percentage of error between the measured field data and the estimated from numerical model. The workflow to implement this technique with real field data was developed in this task assuming a measured strain data for a hypothetical fracture oriented at 40 degree versus all the estimated strains for the hydraulic fractures oriented at different angles as seen in Figure 38. In addition, a particular monitoring location from the fracture center at 6 m (19.68 ft) was selected to extract the estimated strain data. This assumed monitoring point can be considered representative because it is located in the stable zone where less perturbation occurs.

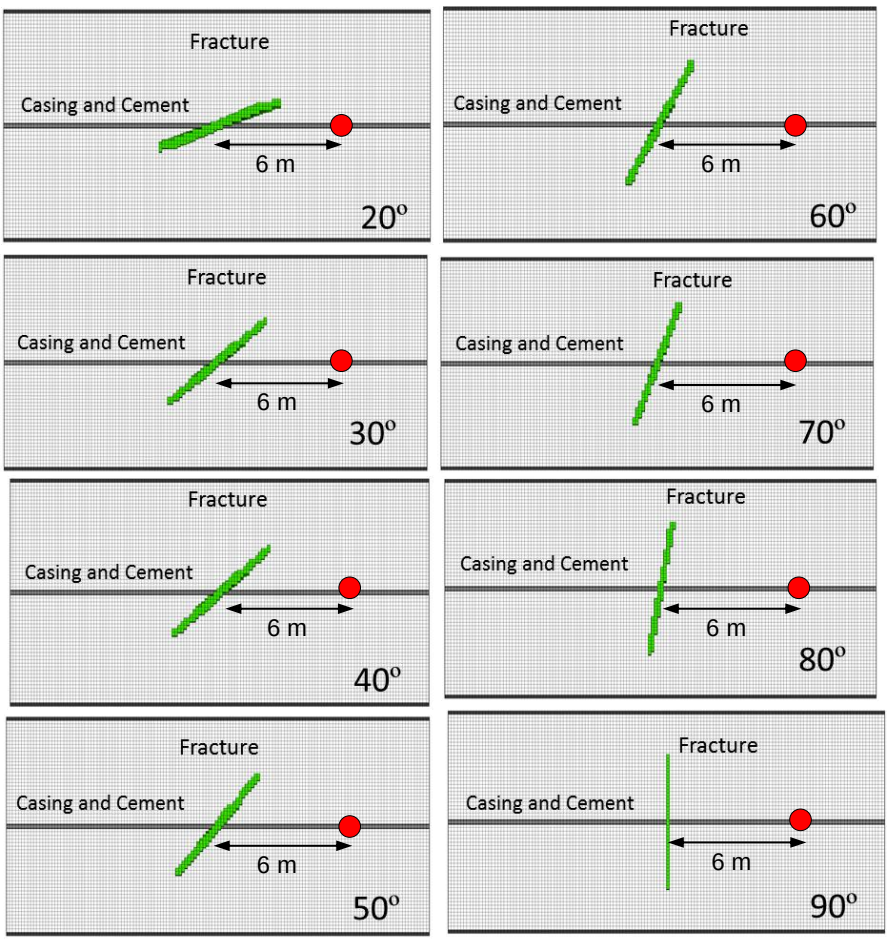

Figure 38: Top view of hydraulic fractures oriented at different angles every 10 degrees with respect to the horizontal well casing and cement and the monitoring location to extract the estimated strain implemented in the inversion technique.

The following equations were applied to calculate the minimized error during the inversion technique process:

Case 1: Error Variation of ± 50% with respect to 50%:

$$Random\ Error1 = -Ref.Error + Random\ Number * Ref.Error * 2 \qquad Eq.\ 14$$

Case 2: Error Variation from 0% to 50%:

$$Random\ Error2 = Random\ Number * Ref.Error \qquad Eq.\ 15$$

$$Measured\ Data = Real\ Value + Real\ Value * Random\ Error \qquad Eq.\ 16$$

$$\%Error = \frac{Measured\ Data - Estimated\ Data}{Measured\ Data} * 100 \qquad Eq.\ 17$$

$$Minimized\ Error = \frac{\sqrt{\sum_1^n Error^2}}{n} \qquad Eq.\ 18$$

Note that a reference error of 50% was assumed and two cases were performed. The first one presents a variation of ± 50% with respect to 50% and the second one a variation from 0% to 50%. A total of 20 random numbers (n) were generated in an excel spreadsheet with a variation from 0 to 1 for each case. Then, the measured data was calculated including the random error. Finally, the minimized error was estimated for each location around borehole named as “A”, “B” and “C”.

Figure 39 through Figure 44 present the minimized error for axial strain along the wellbore-casing-cement interfaces located at A, B and C monitoring points. Overall, the results for *Case 1* suggest a fracture orientation around 40-50 degree with a lower minimized error ranging from 6% to 8%. Meanwhile, the results for *Case 2* present a fracture orientation around 30-40 degree with a lower minimized error below 5%. As seen, the approximation obtained with both cases are reasonable and consistent with the assumed hypothetical fracture orientation of 40 degree.

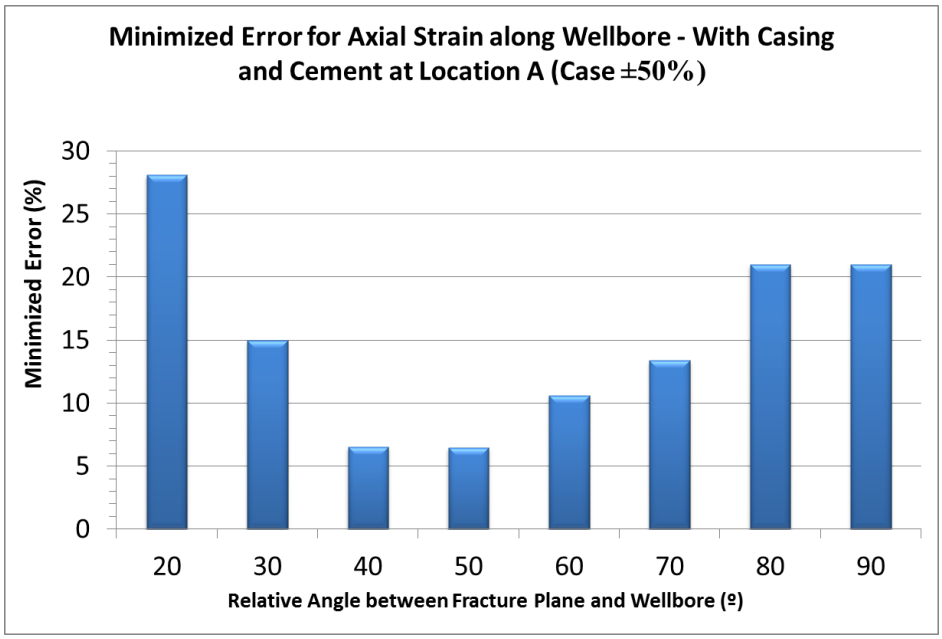

Figure 39: Minimized error for axial strain along wellbore - with casing and cement at location A (Case1 ±50%).

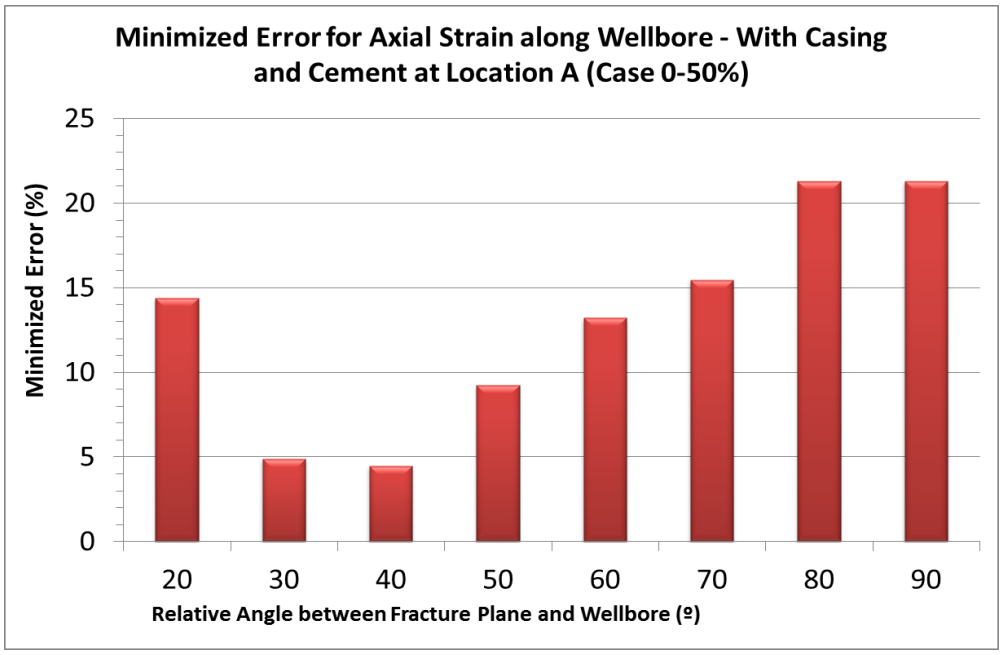

Figure 40: Minimized error for axial strain along wellbore - with casing and cement at location A (Case2 0-50%).

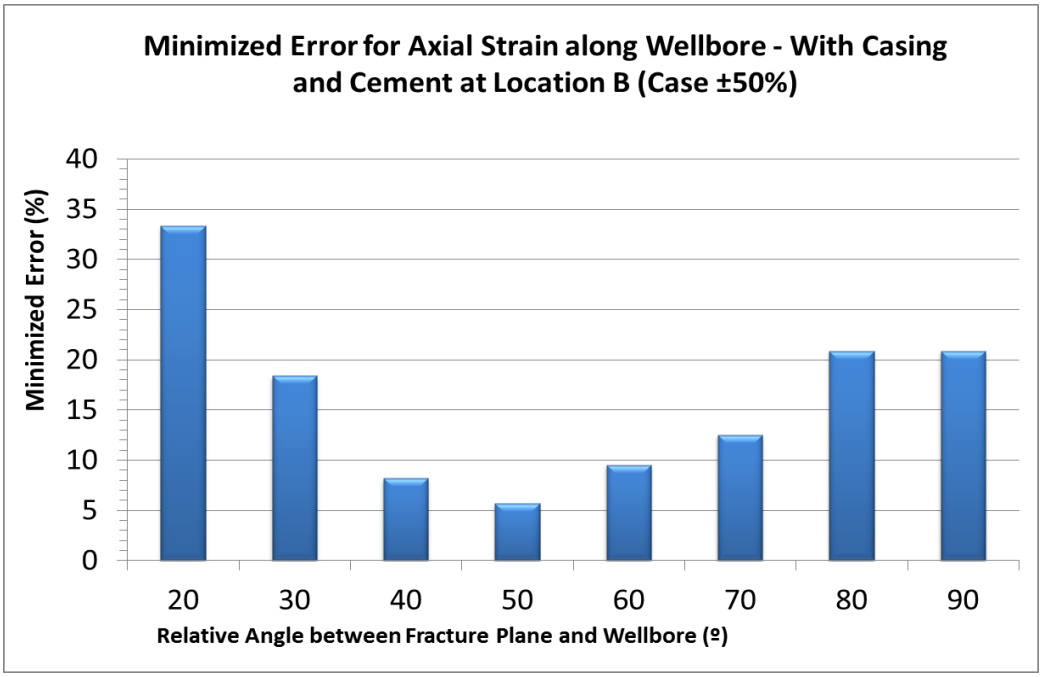

Figure 41: Minimized error for axial strain along wellbore - with casing and cement at location B (Case1 ±50%).

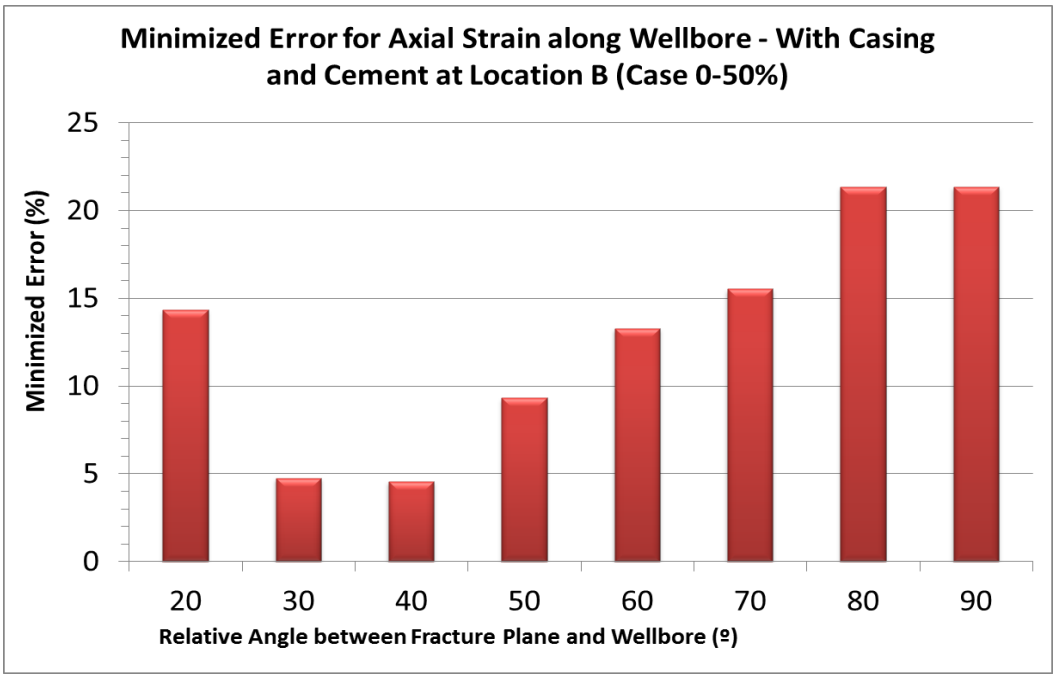

Figure 42: Minimized error for axial strain along wellbore - with casing and cement at location B (Case2 0-50%).

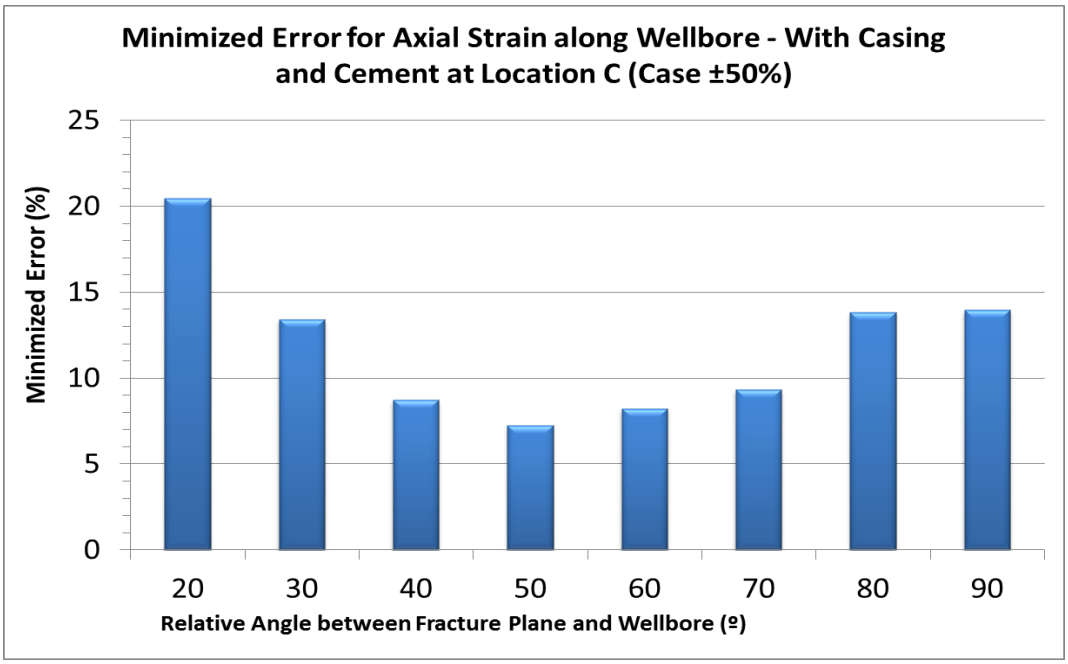

Figure 43: Minimized error for axial strain along wellbore - with casing and cement at location C (Case1 ±50%).

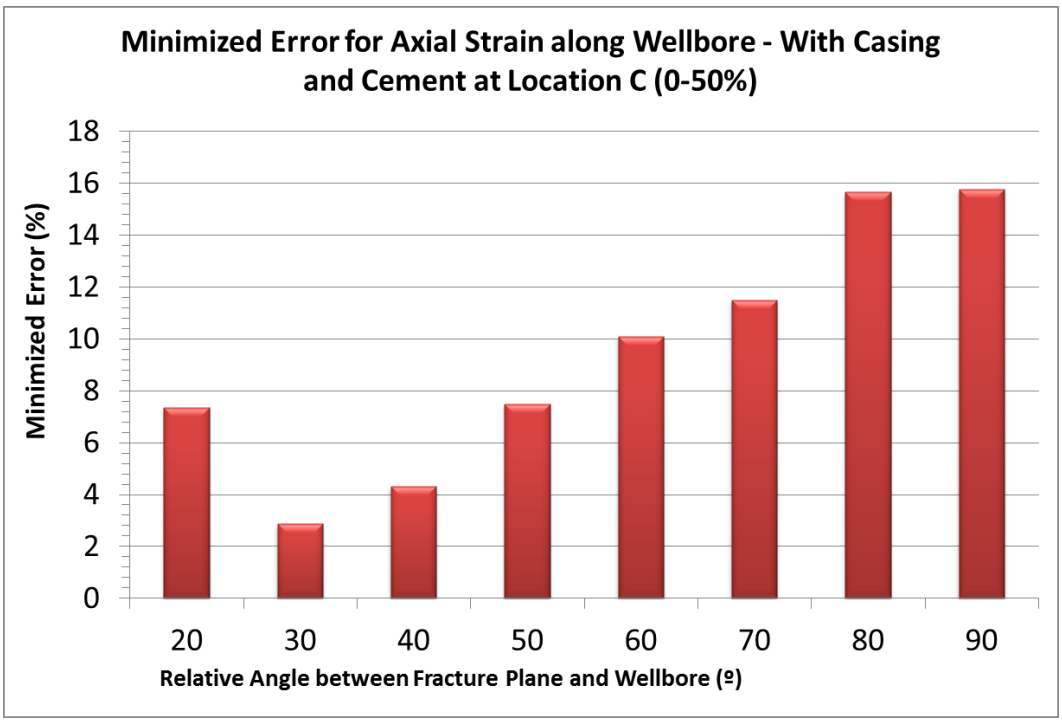

Figure 44: Minimized error for axial strain along wellbore - with casing and cement at location C (Case2 0-50%).

6. Comparison with Field Observation and Documentation (Task 5)

6.1 Field data review

In this task an existing fiber optic cable along a vertical well installed as a distributed temperature sensor (DTS) was used for DAS measurements. This is possible since the fiber optic cable for a DTS and DAS setup is in general the same, where the main differences are only apparent for the setup of the measurement tools at the surface. Though a custom fiber optic cable for DAS measurements can result in a better quality of the measurement (Conway and Mondanos, 2015).

6.1.1 Set up of equipment at TIRE site

The fiber optic (FO) cable used is installed in a vertical well at the Terminal Island Renewable Energy (TIRE) project site (GeoEnvironment Technologies, 2018). Currently there are period waste injections going on in this well at a depth of 1500 m SSL. The FO is imbedded between the 8-5/8" injection casing and the cement; with the purpose of monitoring the temperature outside the well and the reservoir near the perforations (see well schematic with FO, Figure 45).

A ¼-inch FODTS steel capillary tube is attached to opposite sides around the circumference of the injection casing using steel bands similar to hose clamps and Cannon Clamp Centralizers with ¼-inch tube slots. Figure 46 shows an image of a Cannon Clamp Centralizer, similar to the type used for SFI#1. The cable was installed in a U-type system, meaning the cable travels from the surface to the turnaround sub and back to the surface. Centralizers were installed at each casing jointing below 2,927 ft MD. Above this depth, centralizers were installed every other casing joint. A total of 120 casing joints were used for the injection casing string (White, 2015).

Since the injection has started back in 2008 the perforations and the target zone have changed from 1560 m to this shallower depth. Due to this shallower injection depth the fiber optic cable has been destroyed in November 2015 and is since then degrading in measuring accuracy. Nevertheless it still can be used for showing the relative temperature differences along the depth of the well.

.

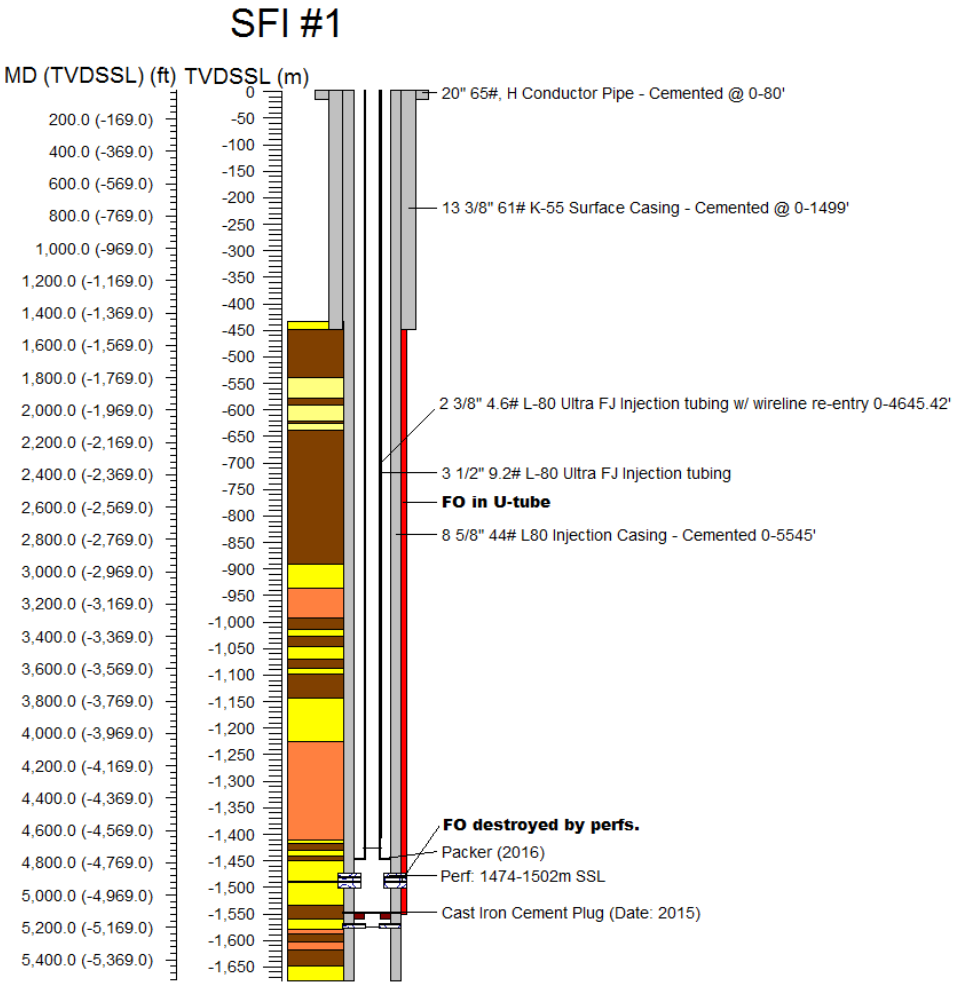

Figure 45: Well Schematic at TIRE site that includes fiber optic cable.

Figure 46: Cannon clamp centralizer with 1/4 inch tube slots (Forum Energy Technologies, 2018.

6.1.2 Measurement procedure

For the purpose of this project the DTS has been converted into a DAS for a 3.5 hour measurement. In preparation to the conversion an ODTR measurement was performed on the multifiber to get information about fiber properties.

On March 12th, 2018 the DTS measurement was stopped at 12:32 and DAS measurement began recording at 15:01 and continued until 17:42. A tap test followed to identify the well head along the fiber length in order to be able to calibrate the fiber meter to the true vertical depth of the fiber along the well bore. DAS measurement was taken at 1 kHz, gauge length was 10m and a reading of strain rate (nm/s) was recorded every meter.

In the following discussion we will refer to the minutes of the measurements where the minutes listed in Table 3 are significant events during the measurement. The injection pressure downhole (BHP) and injection rate of slurry waste are shown for the period of DAS measurement in Figure 47.

Table 3: DAS measurement in the field events

Minute	Time	Event
0	15:01	Start of DAS measurement
151	16:32	Starting step down of injection
182	16:42	Shut-in well
222	17:42	Stop of DAS measurement
224	17:44	Tap Test

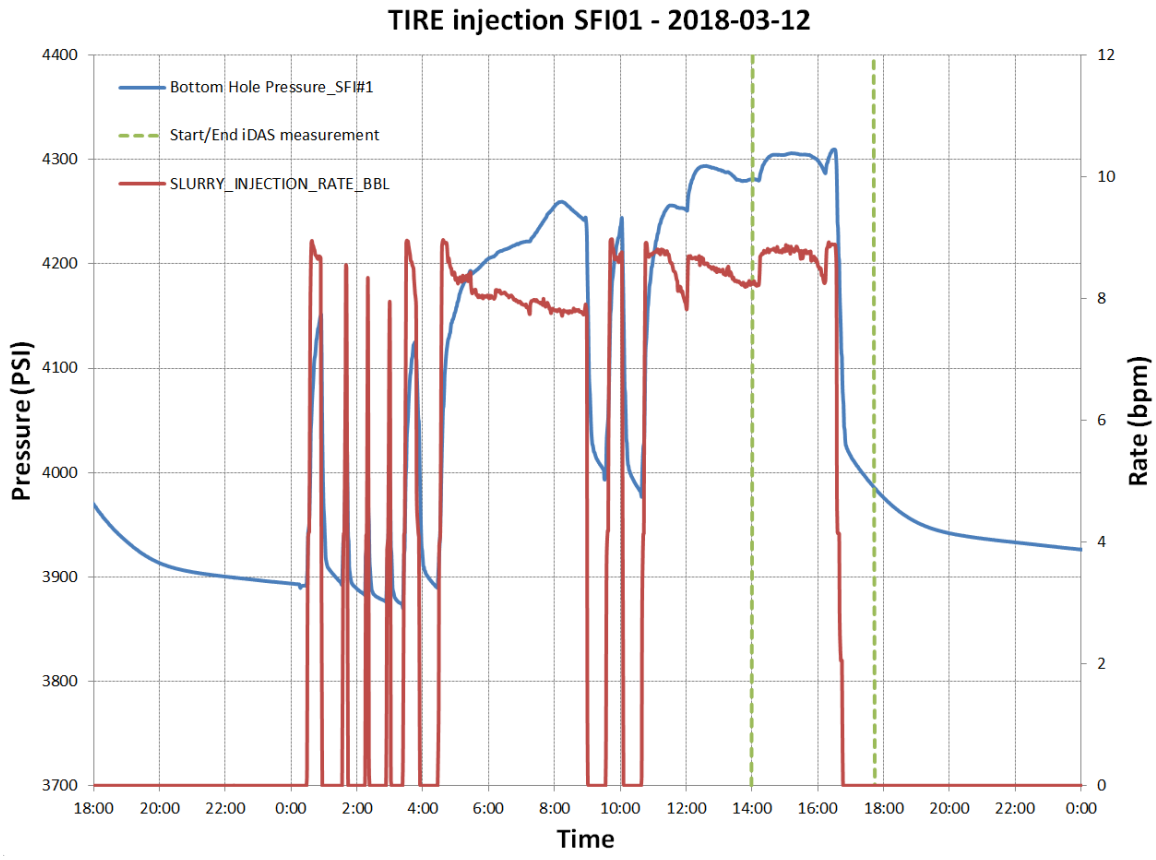

Figure 47: Period of DAS measurement at TIRE.

6.1.3 Data analysis

In the data analysis we want to see if the depth interval of the vertical fracture experiences a different strain during the closing of the fracture as other areas of the reservoir and overburden. From the geomechanical studies performed at the TIRE site, our analyses showed that new vertical fractures are being generated and existing fractures are being re-opened during waste injections.

A primary difference between the setup proposed in the background section (see chapter 2) and the TIRE setup is that the injection well is a vertical well with a fracture being opened along the well – and not perpendicular as expected with a horizontal well set up in HF operations. Thus, the induced axial strain on the FO will mainly be effected by the fracture height.

In general the DAS data shows a high noise response, due to the high injection rate (9 bpm) and also difference in temperature between the injected fluid and surrounding reservoir. Similar conditions are expected in a setup of using DAS to characterize fracture parameters during HF operations.

We start with the analysis of the fracture height using a different approach in the next chapter, before going to the analysis of the DAS measurements.

6.1.3.1 DTS reference analysis

As an indication for the maximum fracture height (= zone of high permeability) we are analyzing the DTS measurement prior the DAS measurement. Figure 48 shows the DTS temperature measurements on March 11, 2018 (a day before the start of FODAS measurement) over 24-hours period for well SFI#1. The time 0:00 (black line) is before the start of injection, with DTS monitoring showing a gradual increase in temperature along the well (from top to bottom) until it reaches a maximum temperature of about 54 C at a depth of 1440 m SSL. Starting from there the temperature decrease again, indicating that the injected waste (originally cooler than the in-situ reservoir temperature) has cooled down the formation up to that point due to liquid penetration in that area. Thus we assume the maximum fracture height possible during injection is about 80 m. The hypothesis to be confirmed now with the DAS measurement is that any strain measured above 1450 m SSL should differ from strain measured in the final meters of the FO.

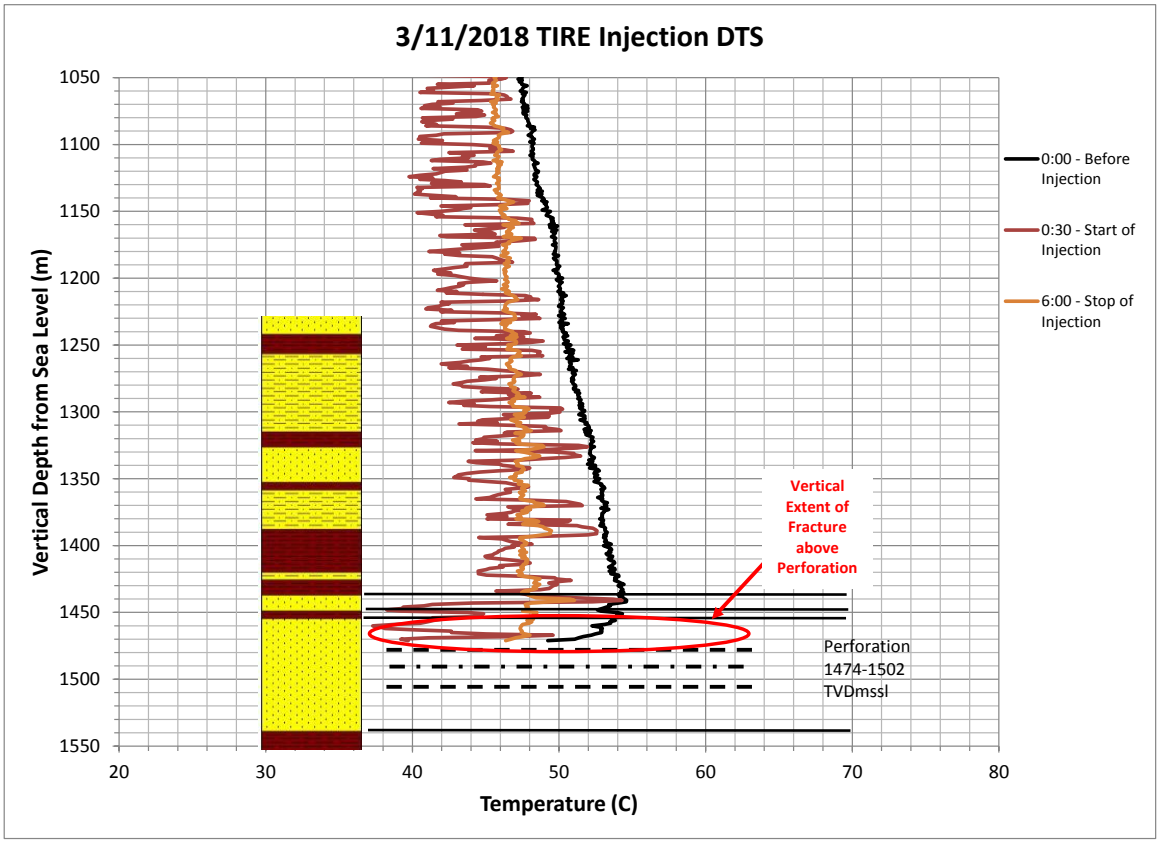

Figure 48: Fiber Optic DTS data over 24-hours period at SFI#1 Injection on March 11, 2018 at TIRE site.

6.1.3.2 DAS data analysis

A workflow has been established to read, process and visualize the large data files from the measurements (~290 MB per minute).

The first step was to identify the well head along the length of the fiber optic cable. The cable starts at the DAS box inside the trailer, runs a while on the surface of the project site until it enters the wellhead. Using a tap test the well head, actually sea level, was identified at about 183 m fiber length, though there was room for interpretation over a length of about 10 m to identify the tap location. Nevertheless assuming 183 m from DAS box to sea level gives a good match with the last reasonable measurement output which is expected at the top of the current perforations, see Figure 49. This figure also shows the high noise in the data, even after the well has been shut-in already for one hour.

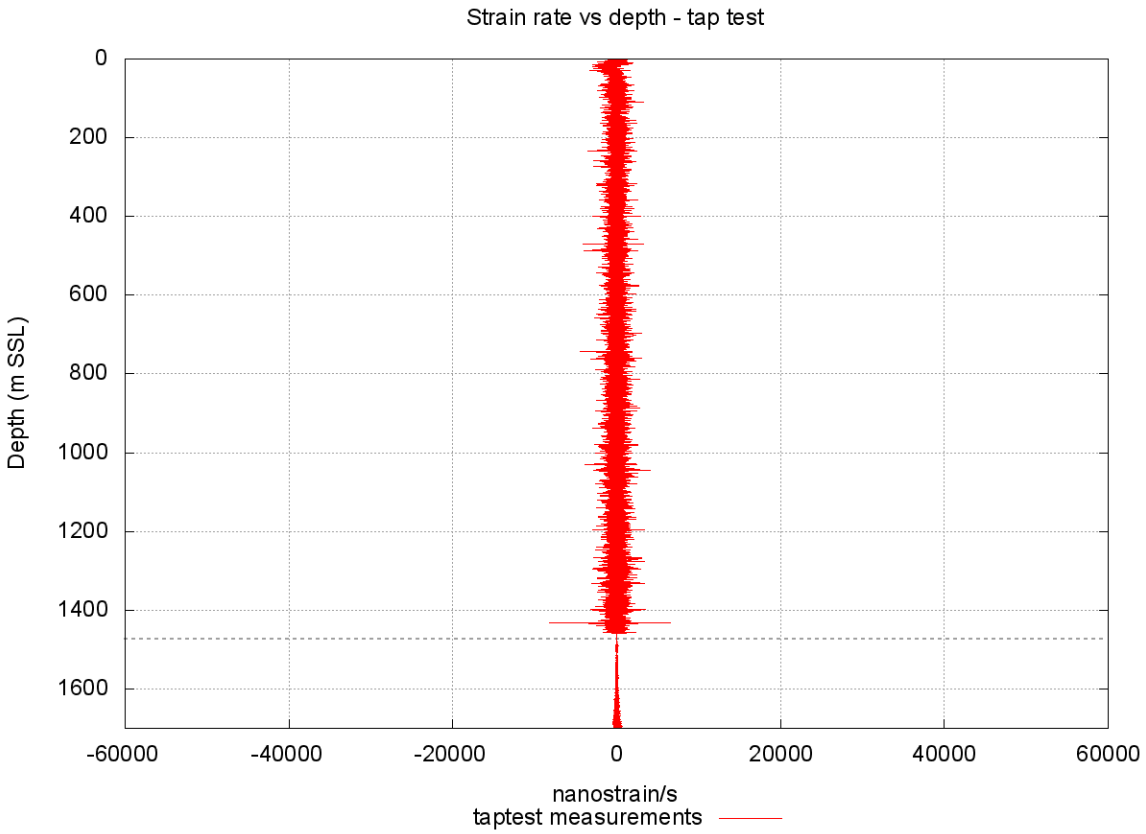

Figure 49: Depth calibrated DAS measurements, dashed horizontal gray line indicating top of perforations.

We are interested in the period of measurement when the fracture closes. Not 100 % comparable, but this can be seen as an opposite of strain induced due to fracture opening. Thus we are going to analyze the period from 150 to 185 min of the field measurement. With no filters yet applied to the raw measurement DAS data, a heat map showing accumulated strain over the period of these 35 min is shown in Figure 50. At the target depth of the injection (-1450 m to -1474 m SSL) we see strain decreasing over the first 10 min after starting the step down (@ 151 min) followed by a period of strain increase (expansion). This is also the depth interval identified as the fracture height. The delta strain observed during the period of step down is on the order of magnitude -200 nanostrain. (-600 contraction + 400 expansion) The accumulated strain above that interval shows a continuous contraction during the period of step down, reaching a maximum of -1200 nanostrain accumulated at a depth of -1280 m SSL. The pressure relieve (about – 320 PSI) in the well could be the cause of the continuous contraction of the FO in between the cement and not fractured formation. While the expansion we see in the interval of the injection sand could be identified as the zone of closing the fracture.

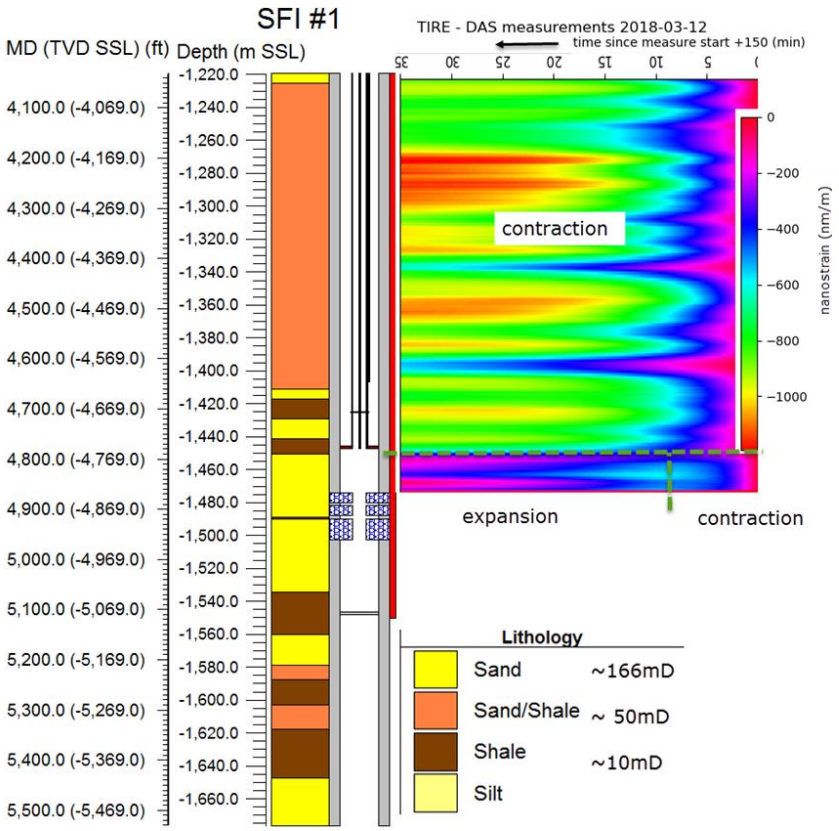

Figure 50: Accumulated strain along the FO for depth interval 1220 m to 1474 m SSL.

6.2 Numerical model under field conditions

A 3D numerical model was set up in Flac3D around well SFI#1. The mesh covers an area of 240 m x 240 m x 250 m (787 ft x 787 ft x 820 ft) with radial elements around the well. A 3D view, vertical cross section through a vertical injection well and horizontal cross section at perforation depth can be seen in Figure 51. Table 4 summarizes the mechanical properties for the field model.

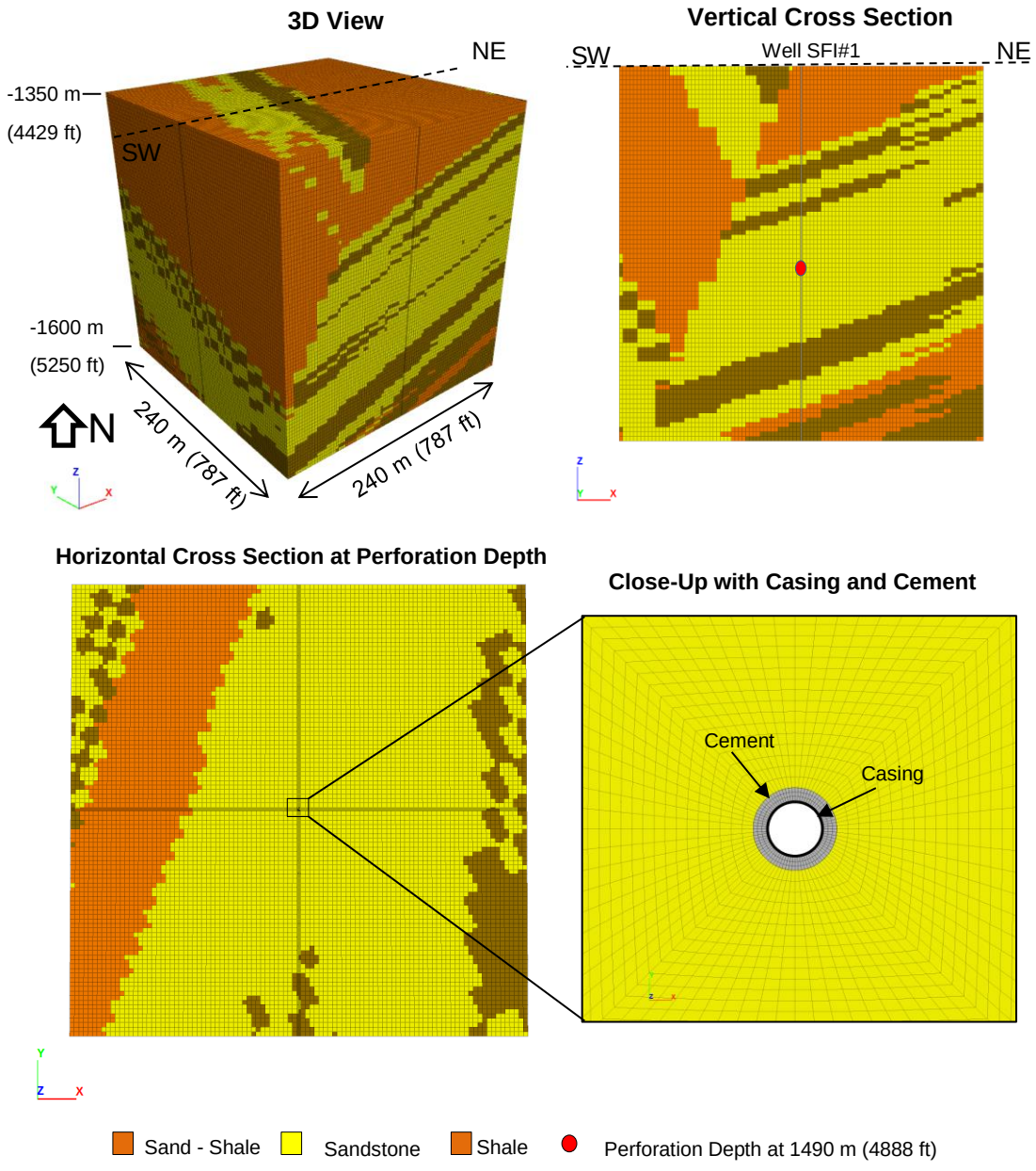

Figure 51: Numerical model mesh with field conditions.

Table 4: Mechanical properties for the field model

Material	Young Modulus	Poisson's ratio	Tenslie Strength	Cohesion	Friction Angle
	Pa	unitless	Pa	Pa	Degree
Sand Shale	3.030e+09	0.24	-	-	-
Sandstone	4.140e+09	0.21	-	-	-
Shale	3.340e+09	0.23	-	-	-
Fracture Zone	4.140e+09	0.21	0	3e6	25
Casing Steel L-80	20.6e12	0.25	-	2.75e8	0
Cement	1.82e9	0.28	1.37e6	2.87e6	4

In order to estimate the strain imposed in the interface between casing and cement, a sensitivity analysis was conducted. Since well SFI#1 is a vertical well, a parallel vertical fracture is expected. Three existing fracture with different height of 20 m (65 ft), 40 m (131 m) and 80 m (262 ft) were considered (see Figure 52). The fracture length was assumed to 100 m (328 ft).

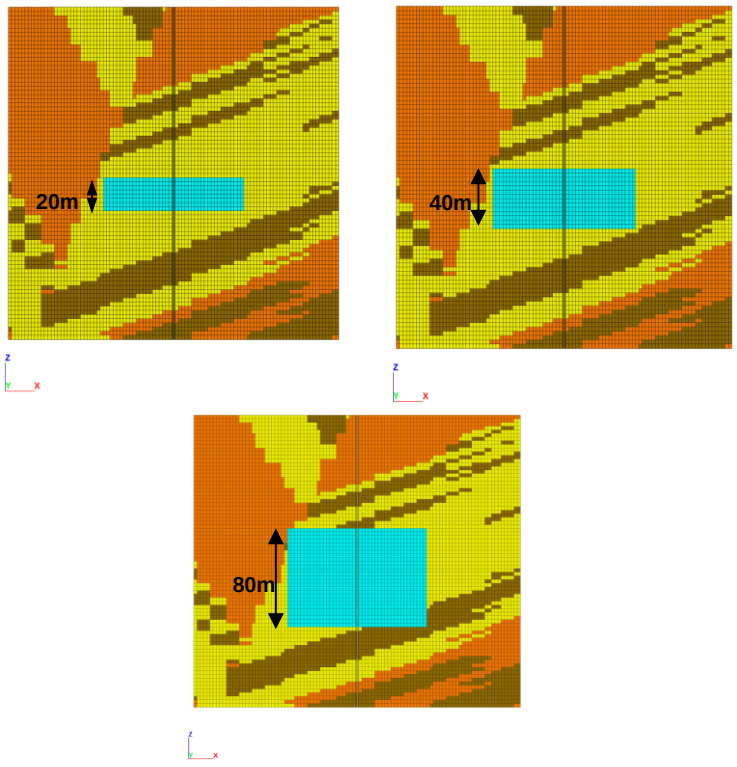

Figure 52: NE-SW cross sections with fracture height of 20m, 40m and 80m.

6.3 Numerical model results

To estimate the strain imposed along the casing during the injection process described in section 6.1 and presented in Figure 47, an average differential pressure of -320 psi was considered during the transition between injection and shut-in. Figure 53 illustrates the results of axial strain versus depth varying the fracture height. Note that these measurements were estimated 90 m up from the top of the perforation interval located at 1490 m. Thus, half height of the fracture was only analyzed. The primary reason is because DAS Fiber Optic cable was damaged at the perforation interval and strain measurements were not conducted below this point. Also, note that the sections with positive strain values correspond to the half fracture section which are under expansion. Nevertheless, a change to negative strain values (contraction) are experienced above the half fracture height. Figure 54 presents NE-SW cross sections showing the axial strain for each fracture height case respectively.

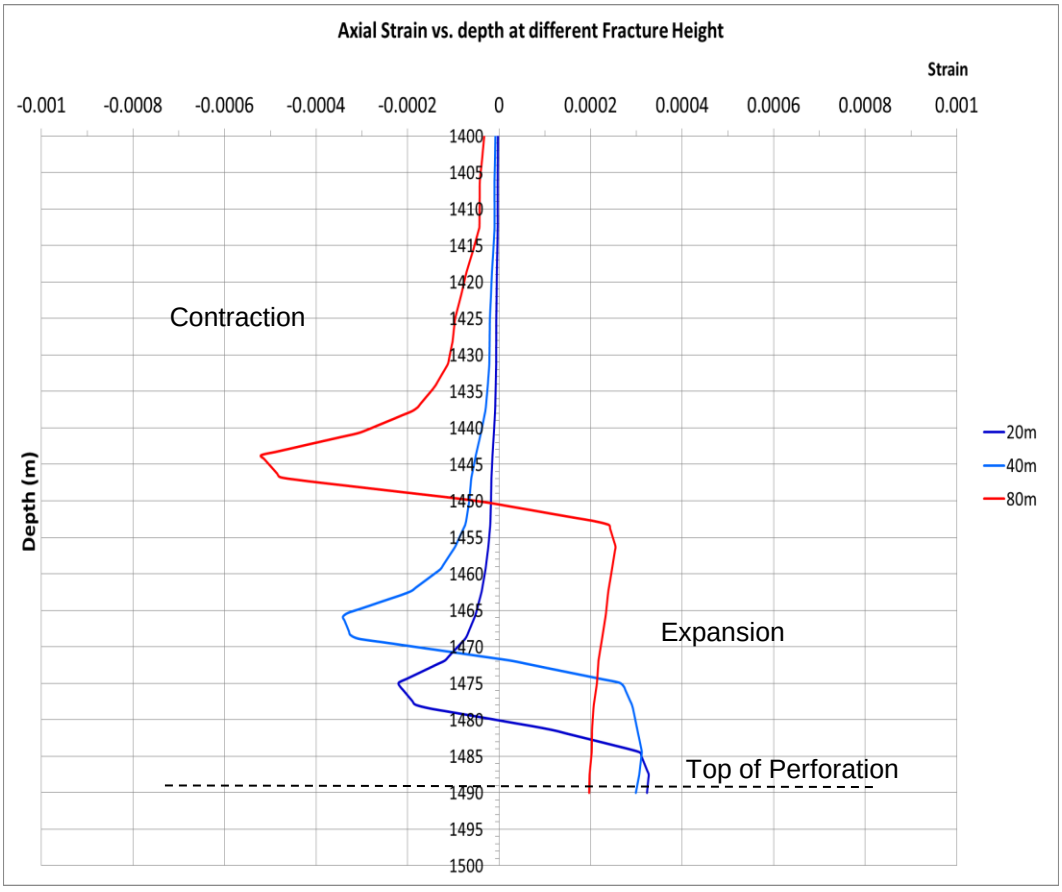

Figure 53: Axial strain versus depth for different fracture height of 20m, 40m and 80m.

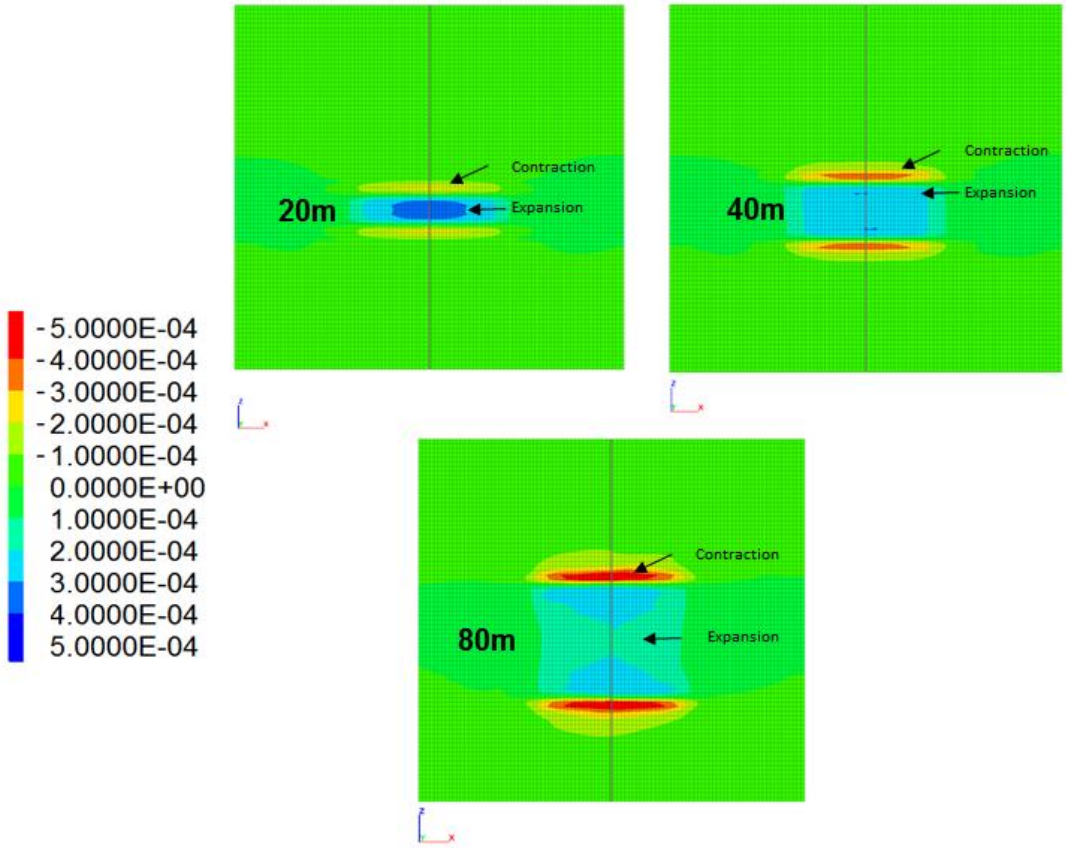

Figure 54: NE-SW cross sections showing axial strain for fracture height of 20m, 40m and 80m.

6.4 Comparison results

After analyzing the field data results shown in Figure 50, we see a similar trend of contraction and expansion as in the numerical models in Figure 53 and Figure 54. The vertical interval of the fracture is expanding vertically, while the depth interval above is vertically contracting. There is a difference in order of magnitude though. While the FO in the field shows an accumulated expansion of 400 nanostrain (min10 to min 35), the numerical model shows around 200 microstrain. The following differences between the field measurement and numerical model need to be considered:

- The numerical model does not include the temperature effect.
- The FO in the field is inside a steel tubing attached to the casing and cemented, while the strain from the numerical model is extrapolated along an interface between steel and cement.
- The numerical model assumes a perfectly cemented well.

- The FO was perforated and damaged from its original length. The measured values provide only qualitative comparison along the fiber, rather than providing accurate quantitative results.
- The FO in the field also measures the acoustic signal sent from the flowing water in the injection tubing. That is not modeled in the numerical model.

Given the various limitations described, we recommend applying the characterization method using a FODAS in an observation well to monitoring and measure the induced strain.

Also, to avoid damage in the fiber optic cable during the perforation (e.g. when setting up multi stage HF scenarios) it is recommended to use oriented perforations. This issue was evidenced in well SFI#1 where it was not possible to obtain strain measurement below the top of the perforation.

7. Conclusions

The objective of this study has been to develop advanced analysis of dynamic and static casing strain monitoring to characterize the orientation and dimensions of hydraulic fractures.

Our current findings and conclusions from the Phase I study include the following:

- A literature review related to the fundamental theoretical and analytical developments of stress and strain imposed by hydraulic fracturing along casing completions and deformation monitoring techniques was performed.

- Analytical solutions have been developed to understand the mechanisms responsible for casing deformation induced by hydraulic fracturing operations.

- After reviewing a range of casing deformation techniques, including fiber optic sensors, borehole ultrasonic tools and electromagnetic tools, we can state that challenges in deployment, data acquisition and interpretation must still be overcome to ensure successful application of strain measurement and inversion techniques to characterize hydraulic fractures in the field.

- Numerical models were developed to analyze induced strain along casing, cement and formation interfaces. The location of the monitoring sensor around the completion, mechanical properties of the cement and its condition in the annular space can impact the strain measurement.

- Field data from fiber optic sensors were evaluated to compare against numerical models. A reasonable match for the fracture height characterization was obtained.

Discrepancies in the strain magnitude between the field data and the numerical model was observed and can be caused by temperature effects, the cement condition in the well and the perturbation at the surface during injection.

- To avoid damage in the fiber optic cable during the perforation (e.g. when setting up multi stage HF scenarios), oriented perforations technologies are suggested. This issue was evidenced in the analyzed field data, where it was not possible to obtain strain measurement below the top of the perforation. This presented a limitation to characterize the entire fracture geometry.

- The comparison results from numerical modeling and field data for fracture characterization shows that the proposed methodology should be validated with alternative field demonstration techniques using measurements in an offset observation well to monitor and measure the induced strain. We propose to expand on this research in Phase II with a further study of multi-fracture characterization and field demonstration for horizontal wells.

8. References

– Appel M., Dria D., Freeman J., Rambow F., Shuck M., 2007. "Real-time fiber-optic casing imager". SPE 109941 paper presented at the SPE Annual Technical Conference and Exhibition, California, U.S.A, November, 2007.

– Bao S., Fu M., Hu S., Gu Y., Low H., 2016. "A review of the metal magnetic memory technique". 35th International Conference on Ocean, Offshore and Arctic Engineering OMAE2016, Busan, South Korea, June 19-24, 2016.

– Brill T.M., Le Calvez J., Demichel C., Nichols E., Zapata F., 2012. "Electromagnetic casing inspection tool for corrosion evaluation". International Petroleum Technology Conference, Bangkok, Thailand, 7-9 February 2012.

– Callister W, 2005. "Fundamentals of materials science and engineering". John Wiley & Sons, Inc. Danvers, MA. Accessible online from: https://en.wikipedia.org/wiki/Burgers_vector, Oct, 2017.

– Castaneda C., Higuera J., Portela F., Benavides M., Valstart D., Banerjee S., 2014. "Corrosion monitoring with EM induction tool in 3 outer casing strings through a 7 inch Chrome production tubing scenario". SPE 168277 paper presented at the SPE Annual Technical Conference and Exhibition, The Woodland, Texas, March, 25-26, 2014.

– Conway C., and Mondanos M., 2015. "An introduction to fibre optic Intelligent Distributed Acoustic Sensing (iDAS) technology for power industry applications". In

Proceedings 9th International Conference on Insulated Power Cables France, Versailles 21-25 June, 2015, Volume 2125, p. 16.

- Davis P, 1983. "Surface deformation associated with a dipping hydrofracture". Journal of Geophysical Research, Vol. 88, No. B7, Pages 5826-5834, July 10, 1983.

- Ekie S., Hadinoto N., and Raghavan R., 1977. "Pulse-testing of vertically fractured wells". Paper presented at the SPE Annual Technical Conference and Exhibition, Denver, Oct. 9-12 1977.

- Forum Energy Technologies, 2018. Thermoplastic Centralizer - Forum Energy Technologies, Retrieved from http://www.f-e-t.com/products/completions/well-completion/protection-systems/specialty-products/thermoplastic-centralizer, (accessed 4/20/2018).

- Frisch G. and Mandal B, 2001. "Advanced ultrasonic scanning tool and evaluation methods improve and standardize casing inspection". SPE 71399 paper held in SPE Annual Technical Conference and Exhibition, New Orleans, Louisiana, 30 September–3 October 2001.

- Halliburton Service, 2017. "Multifinger Imaging Tool (MIT)". Accessed from: http://www.baroididp.com/public/lp/contents/Data_Sheets/web/H/Multifinger-Imaging-Tool-MIT.pdf, Nov,2017.

- Harold L., Ahmed R., Edwards J., Soriano V., Friesenhahn J., 2015. "Intelligent Casing-Intelligent Formation Telemetry (ICIFT) System". University of Oklahoma, 2015.

- Kittel C., 1996. "Introduction to solid state physics". 7th edition, John Wiley & Sons, Inc, pp 592–593.

- Koelman J., Lopez J., Potters J., 2012. "Optical fibers: the neurons for future Intelligent wells". SPE 150203 paper presented at the Intelligent Energy International Conference, Netherlands, March, 2012.

- Lian Z., Yu H., Lin T., Guo J., 2015. "A study on casing deformation failure during multi-stage hydraulic fracturing for the simulated reservoir volume of horizontal shale wells". Journal of Natural Gas Science and Engineering, 23 (2015), 538-546.

- Lin T., Yu H., Lian Z., Sun B., 2017. "Casing failure mechanism during volume fracturing: A case study of shale gas well". Journal of Advances in Mechanical Engineering, Vol. 9 (8), 1-9, 2017.
- Liu H., 2017. "Principles and applications of well logging". Springer, 2017.

- Lumens G. E, 2014. “Fibre-optic sensing for application in oil and gas wells”. Eindhoven University of Technology.

- Mindlin R., 1936. “Force at a point in the interior of a semi-infinite solid”, Physics 7, 195-202.

- Minardo A., Coscetta A., Pirozzi S., Zeni L., 2015. “Brillouin optical time domain analysis sensor for active vibration control of a cantilever beam”. Hindawi Publishing Corporation, Journal of Sensors, 2015.

- Molenaar M., Cox B., 2013. “Field cases of hydraulic fracture stimulation diagnostics using fiber optic distributed acoustic sensing (DAS) measurements and analyses”. SPE 164030 paper presented at the Middle East Unconventional Gas Conference and Exibition, Muscat, Oman, January, 2013.

- Okada Y., 1985. “Surface deformation due to shear and tensile faults in a half-space”. Bulletin of the Seismological Society of America, Vol. 75, No. 4, pp. 1135-1154, August 1985.

- Pearce J., Rambow F., Shroyer W., Huckabee P., De Jongh H., Dria D., 2009. “High Resolution, Real-Time Casing Strain Imaging for Reservoir and Well Integrity Monitoring: Demostration of Monitoring Capability in a Field Installation”. SPE 124932 paper presented at the Annual Technical Conference and Exhibition, Louisiana, 2009.

- Pinto H., Braga A., Gouvea P., 2013. “Well integrity monitoring: challenges and perspectives” OTC 24515 paper presented at the Offshore Technology Conference, Brazil, October, 2013.

- Roylance D., 2001. “Pressure vessels”. Massachusett Institute of Technology, 2001.

- Soga K., Mohamad H., Bennett P., 2008. “Distributed fiber optics strain measurements for monitoring geotechnical structures”. International Conference on Case Histories in Geothermal Engineering, Arlington, VA, August, 2008.

- Steketee J., 1958. “Some geophysical applications of the elastic theory of dislocations”. Journal of Physic, 36, 1168-1198.

- Sun B., Fan J., Wen D., Zhao K., Hu Z., 2014. “A Design of magnetic memory Sensor of oil well casing damage detection”. Information Technology Journal, Beijing, 2014.
- Tiab D., Aboblse E. O., 1989. “Determining fracture orientation from pulse testing”. Paper presented at the SPE Annual Technical Conference and Exhibition held in New Orleans, Sept. 26-29.

- White A., 2015, “Passive and active fiber optic distributed temperature sensing for downhole lithologic and porosity characterization at Terminal Island, Los Angeles, California”. California State University, Long Beach, 166 p.

- Yang X. and Davis P., 1986. “Deformation due to a rectangular tension crack in an elastic half-space”. Bulletin of the Seismological Society of America, Vol. 76, No. 3, pp. 865-881, June 1986.

- Zemanek J., Caldwell R. L., Glenn E. E., Jr., Holcomb S. V., Norton L. J., and Strauss D., 1969. “The borehole televiewer: a new logging concept for fracture location and other types of borehole inspection”. J. Pet. Tech. (June 1969) 762-774.

- Zhaowei C., Lin S., Degui X., 2016. “Mechanism of casing deformation in the Changning-Weiyuan national shale gas demonstration area and countermeasures”. CNPC Drilling Research Institute, 2016.

- Zhou Z., He J., Huang M., He J., Chen G., 2010. “Casing pipe damage detection with optical fiber sensors: a case study in oil well constructions”. Hindawi Publishing Corporation Advances in Civil Engineering.